Evidence of Strong Guest–Host Interactions in Simvastatin Loaded in Mesoporous Silica MCM-41

Teresa Cordeiro, Inês Matos, Florence Danède, João C. Sotomayor, Isabel M. Fonseca, Marta C. Corvo, Madalena Dionísio, María Teresa Viciosa, Frédéric Affouard, Natália T. Correia

pharmaceutics

MDPI

Article

Evidence of Strong Guest–Host Interactions in Simvastatin Loaded in Mesoporous Silica MCM-41

Teresa Cordeiro [1], Inês Matos [1], Florence Danède [2], João C. Sotomayor [1], Isabel M. Fonseca [1], Marta C. Corvo [3], Madalena Dionísio [1], María Teresa Viciosa [4], Frédéric Affouard [2] and Natália T. Correia [2,*]

[1] LAQV-REQUIMTE, Department of Chemistry, NOVA School of Science and Technology, Universidade Nova de Lisboa, 2829-516 Caparica, Portugal; teresa.m.cordeiro@gmail.com (T.C.); ines.matos@fct.unl.pt (I.M.); sotomayor@fct.unl.pt (J.C.S.); blo@fct.unl.pt (I.M.F.); madalena.dionisio@fct.unl.pt (M.D.)

[2] Univ. Lille, CNRS, INRAE, Centrale Lille, UMR 8207 - UMET - Unité Matériaux et Transformations, F-59000 Lille, France; florence.danede@univ-lille.fr (F.D.); frederic.affouard@univ-lille.fr (F.A.)

[3] i3N | Cenimat, Materials Science Department, NOVA School of Science and Technology, NOVA University, 2829-516 Caparica, Portugal; marta.corvo@fct.unl.pt

[4] Centro de Química Estrutural, Institute of Molecular Sciences, Department of Chemical Engineering, Instituto Superior Técnico, Universidade de Lisboa, Av. Rovisco Pais, 1049-001 Lisbon, Portugal; teresaviciosa@ist.utl.pt

* Correspondence: natalia.correia@univ-lille.fr

Abstract: A rational design of drug delivery systems requires in-depth knowledge not only of the drug itself, in terms of physical state and molecular mobility, but also of how it is distributed among a carrier and its interactions with the host matrix. In this context, this work reports the behavior of simvastatin (SIM) loaded in mesoporous silica MCM-41 matrix (average pore diameter ~3.5 nm) accessed by a set of experimental techniques, evidencing that it exists in an amorphous state (X-ray diffraction, ssNMR, ATR-FTIR, and DSC). The most significant fraction of SIM molecules corresponds to a high thermal resistant population, as shown by thermogravimetry, and which interacts strongly with the MCM silanol groups, as revealed by ATR-FTIR analysis. These findings are supported by Molecular Dynamics (MD) simulations predicting that SIM molecules anchor to the inner pore wall through multiple hydrogen bonds. This anchored molecular fraction lacks a calorimetric and dielectric signature corresponding to a dynamically rigid population. Furthermore, differential scanning calorimetry showed a weak glass transition that is shifted to lower temperatures compared to bulk amorphous SIM. This accelerated molecular population is coherent with an in-pore fraction of molecules distinct from bulklike SIM, as highlighted by MD simulations. MCM-41 loading proved to be a suitable strategy for a long-term stabilization (at least three years) of simvastatin in the amorphous form, whose unanchored population releases at a much higher rate compared to the crystalline drug dissolution. Oppositely, the surface-attached molecules are kept entrapped inside pores even after long-term release assays.

Keywords: simvastatin; amorphous state; molecular mobility; drug release; drug-carrier multiple interactions; drug delivery development

Citation: Cordeiro, T.; Matos, I.; Danède, F.; Sotomayor, J.C.; Fonseca, I.M.; Corvo, M.C.; Dionísio, M.; Viciosa, M.T.; Affouard, F.; Correia, N.T. Evidence of Strong Guest–Host Interactions in Simvastatin Loaded in Mesoporous Silica MCM-41. *Pharmaceutics* **2023**, *15*, 1320. https://doi.org/10.3390/pharmaceutics15051320

Academic Editor: Franc Vrečer

Received: 31 March 2023
Revised: 15 April 2023
Accepted: 20 April 2023
Published: 22 April 2023

1. Introduction

Simvastatin, [(1S,3R,7S,8S,8aR)-8-[2-[(2R,4R)-4-hydroxy-6-oxooxan-2-yl]ethyl]-3,7-dimethyl-1,2,3,7,8,8a-hexahydronaphthalen-1-yl]2,2-dimethylbutanoate, belonging to the antihyperlipidemic therapeutic class [1], is one of the most prescribed pharmaceutical drugs worldwide, including in the USA [2], and is used for the treatment of hypercholesterolemia [3,4] and dyslipidemia as an adjunct to diet.

Simvastatin (SIM) is a Class II drug according to the Biopharmaceutics Classification System. It is acceptably permeable [5] but is poorly water soluble [6] (7.25×10^{-2} mg L^{-1}

at 25 °C in water [7], 24.4 mg L^{-1} in phosphate buffer at pH 6.8 and 37 °C after 48 h [8]), highly limiting its oral bioavailability (<5% [3,4]). Therefore, it would be beneficial if the solubility and/or dissolution rate were improved [9,10]. This is in line with the current goals of the pharmaceutical sciences and industry that seek to improve the effectiveness of already existing drugs through new formulations instead of investing in the design and synthesis of new molecules, which is costly and time-consuming [11].

In this context, alternative SIM administration routes were adopted [12–14], and several strategies have been addressed to enhance its solubility as drug particles reduction [15,16], solid lipid nanoparticles [17], solid surface dispersions [18], co-solvent evaporation with a hydrophilic polymer [19], emulsions and self-emulsifying systems [20,21], spray drying [22], and complexation [8,23].

Among the different approaches, amorphization has also been successfully used to improve SIM solubility [24]. Nevertheless, despite the relatively stabilization claimed for amorphous SIM due to strong hydrogen bonding [25] and high configurational entropy [26], it can convert to the stable crystalline counterpart depending on the way it was prepared [27], including particle size [28], or even to undergo chemical degradation as reported for mechano-activated amorphization [29]. Co-amorphization [30], solid dispersions [31], and the loading in glass nano-tube scaffolds [32] and mesoporous matrices [33,34] have been used to overpass the thermodynamic instability of the out-of-equilibrium amorphous form; however, recrystallization could occur depending on the pore diameter [34].

In the present study, amorphization of simvastatin (see structure in Scheme 1) was achieved through incorporation in hexagonally ordered MCM-41 mesoporous silica with high specific surface area, pore volume and an average pore diameter ~3.5 nm, which was used earlier as a drug carrier [35]. These 100% silica matrices have the added benefit of low or no cytotoxicity [33,36–39]. The guest behavior was investigated by a set of experimental techniques: thermogravimetric analysis (TGA), Powder X-ray Diffraction (PXRD), solid-state Nuclear Magnetic Resonance (ssNMR), Attenuated Total Reflectance Fourier Transform InfraRed spectroscopy (ATR-FTIR), and Differential Scanning Calorimetry (DSC). Several studies in the literature report a significant solubility enhancement of amorphous SIM relative to its crystalline counterpart by a factor of two [28], five [24], ten [22], or even twelve thousand [23] times. Nevertheless, if amorphization is achieved by incorporation in a mesoporous matrix, its release could be slowed, or it can be retained by adsorption inside pores, acting as an indicator of the strength of guest–host interactions. In this context, SIM-MCM-41 interactions were thoroughly investigated by ATR-FTIR, and the way it is distributed in the matrix was inferred by DSC and molecular dynamics (MD) simulations. MD provided a picture of SIM distribution and anchoring inside pores, which, together with the molecular mobility of the loaded drug, are critical factors that could perform a role in the release mechanism [40]. The dynamical behavior of loaded SIM was probed by dielectric relaxation spectroscopy (DRS) that monitors reorientational motions of permanent dipoles under the influence of an external oscillating electrical field [41]. Studies providing the dielectric characterization of simvastatin-based delivery systems are scarce [34] and the same is true for the bulk amorphous drug [26,34].

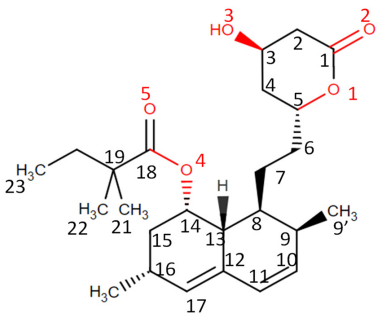

Scheme 1. Chemical structure of simvastatin: oxygen atoms numbered in red and carbon atoms numbered in black according to ref. [26].

The knowledge of the different relaxational modes active inside pores, SIM physical state, guest–host interactions, and distribution among the matrix will allow a better understanding of its release profile, contributing to a rational design of drug delivery systems.

2. Materials and Methods

2.1. Materials

Simvastatin ($C_{25}H_{38}O_5$) was kindly gifted by Mepha, Lda. (CAS number 79902-63-9, >99% assay according to the supplier, molar mass of 418.6 g mol^{-1}). It was used without further purification.

MCM-41 (100% Si) matrix, presenting an ordered mesoporous structure, was synthesized as described in reference [35].

2.2. Methods

2.2.1. Matrix Textural Analysis

Nitrogen (N_2) adsorption analysis through the N_2 adsorption–desorption at −196 °C was used to determine the textural properties of the MCM-41 matrix before and after SIM loading. The specific surface area was determined with the Brunauer–Emmett–Teller (BET) method from the linear portion of the adsorption isotherm (relative pressures between 0.05 and 0.3 [42]). Total pore volume was estimated by calculating the amount of nitrogen adsorbed at the relative pressure P/P_0 = 0.95 and the pore size distribution was determined by Brunauer–Joyner–Halenda (BJH) considering that pores are cylindrical and using the desorption branch data of the isotherm [43].

2.2.2. Drug Loading

Prior to SIM loading, the mesoporous silica matrix (~150 mg of MCM-41) was submitted to heating at 150 °C, at vacuum pressure (10^{-4} bar) for 8 h, by immersion of the glass cell in a paraffin bath, to remove water and any impurity. After cooling to room temperature, a solution of 92 mg of simvastatin dissolved in 2 mL of chloroform was incorporated into the silica matrix under a vacuum. The solvent was evaporated under gentle stirring for 3 days at room temperature. The SIM-MCM-41 ratio used here was found after optimizing the loading conditions to avoid drug outside pores. Loaded SIM sample (designated as SIM:MCM) was prepared in a single batch allowing its characterization by all techniques.

2.2.3. Thermogravimetric Analysis (TGA)

Thermogravimetric measurements (samples of ~1–4 mg) were completed from 22.5 °C to 550 °C, at a heating rate of 5 °C min^{-1}, using a TGA Q500 apparatus (TA Instruments Inc., Guyancourt, France), under a highly-pure nitrogen atmosphere (sample purge flow rate of 60 mL min^{-1}). The temperature and mass reading were calibrated using the Curie point of the nickel standard and using equibalance tare weights (provided by TA Instruments Inc), respectively.

The drug loading (w/w) percentage was calculated according to Equation (1).

$$drug\ loading\ (w/w)\% = \frac{mass\ simvastatin}{mass\ simvastatin + mass\ silica\ matrix} \times 100 \quad (1)$$

The filling degree (v/v) was estimated according to Equation (2), taking into account the loading percentage determined by thermogravimetry (Equation (1)) the total pore volume and density of crystalline simvastatin (1.172 g cm^{-3} [44]).

$$filling\ \% = \frac{m_{SIM}(\mathrm{g})\rho(\mathrm{g\ cm^{-3}})}{pore\ volume(\mathrm{g\ cm^{-3}})m_{silica}(\mathrm{g})} \times 100 \quad (2)$$

2.2.4. Attenuated Total Reflectance-Fourier Transform Infrared (ATR-FTIR) Spectroscopy

ATR-FTIR spectra (400–4000 cm^{-1}) were recorded using a Cary 630 FTIR spectrometer equipped with a diamond attenuated total reflectance, ATR (Agilent Technologies, Santa

Clara, CA, USA), a dTGS detector thermoelectrically cooled, and KBr standard beam splitter. All spectra were recorded at room temperature via ATR method (resolution of 1 cm^{-1} and 16 scans). The spectrum corresponding to which is designated bulk amorphous SIM was collected after cooling a melted sample of crystalline SIM inside a DSC pan.

2.2.5. Powder X-ray Diffraction (PXRD)

The X-ray diffraction analysis ($5° < 2\theta \leq 60°$; scan step = 0.0167 s/°) was performed at room temperature using a PANalytical X'Pert pro MPD diffractometer equipped with a Cu X-ray tube ($\lambda_{Cu\,K\alpha}$ = 1.54056 Å) and the X'celerator detector. The powder samples were enclosed in a Lindemann glass capillary (diameter 0.7 mm), which was rotated during data collection.

2.2.6. Solid-State Nuclear Magnetic Resonance (ssNMR)

Solid-state ^{13}C MAS spectra were acquired at room temperature using a 7 T (300 MHz) spectrometer (AVANCE III Bruker) operating at 75 MHz (^{13}C) and equipped with a BBO probehead. The samples were spun at the magic angle at a frequency of 5 kHz in 4 mm diameter rotors. ^{13}C MAS NMR spectra were acquired with proton cross-polarization (CP/MAS) with a contact time of 1.2 ms, a recycle delay of 2.0 s, and the number of scans was 5000.

2.2.7. Differential Scanning Calorimetry (DSC)

DSC measurements were performed using a DSC Q2000 operating in the Heat Flow T4P option and equipped with an RCS cooling system (TA Instruments Inc., Tzero DSC technology). The measurements were carried out under a very pure nitrogen atmosphere (flow rate of 50 mL min^{-1}). Samples of ~5 mg were encapsulated in aluminum Tzero hermetic pans with a Tzero perforated lid to allow evaporation of water. The samples were first subjected to two cycles of cooling and heating (from −90 to 170 °C) at a rate of 10 °C min^{-1}. Subsequently, a cooling and heating cycle was carried out at a rate of 30 °C min^{-1}.

2.2.8. Dielectric Relaxation Spectroscopy (DRS)

SIM:MCM composite and neat SIM were analyzed through dielectric relaxation spectroscopy. In short, for a material containing permanent molecular dipoles, the application of an external oscillating electrical field will cause the fluctuation of such dipoles with a preferential alignment, originating what is called orientational polarization. This is not an instantaneous response as it occurs in optical spectroscopies; instead, a phase lag exists between the stimulus—the variant electric field—and the build-up of orientational polarization. The stimulus-response relationship is described mathematically by the formalism of complex numbers [45], and therefore, a complex permittivity is defined as a function of an angular frequency, ω, $\varepsilon^*(\omega) = \varepsilon'(\omega) - i\varepsilon''(\omega)$; the real component quantifies the energy stored by the material, and in the imaginary part, the energy is dissipated by the dipoles which can no longer follow the oscillating electric field [41,45].

A sample of each material, SIM and SIM:MCM, was sandwiched with two silica spacers (50 μm of thickness) in between two gold-plated electrodes of parallel plate capacitors. The sample cell (BDS 1200) was placed on a cryostat (BDS 1100), and the temperature (±0.5 °C) was controlled by Quatro Cryosystem. The real and imaginary components of the complex dielectric function, $\varepsilon^*(f) = \varepsilon'(f) - i\varepsilon''(f)$ (where $f = \omega/(2\pi)$ is the frequency of the applied oscillating electric field), were measured using an Alpha-N independence analyzer. Isothermal dielectric spectra, from 10^{-1} to 10^6 Hz, were acquired over two runs, from −95 °C to 100 °C (first run) and from −95 °C to 165 °C (second run). All modules were supplied by Novocontrol Technologies GmbH.

2.2.9. In Vitro Drug Dissolution and Drug Release Studies

A calibration curve was constructed with simvastatin solutions in concentrations ranging from 2 to 14 mg L^{-1}, in phosphate buffer (5 mg L^{-1}; pH = 6.8). A Thermo Scientific Evolution spectrometer and quartz cells were used for the acquisition of the absorption spectra over a wavelength range from 190 to 400 nm. The readings at 231, 238, and 247 nm were taken to build 3 calibration curves whose linearity (r^2 > 0.99 for all the 3 chosen wavelengths) confirms Beer's law applicability.

The dissolution assays of simvastatin were carried out by dissolving 2.85 mg of neat crystalline SIM in 200 mL of the phosphate-buffered solution. For the drug release trials, SIM:MCM was weighted to ensure that the sample contains 2.77 mg of SIM based on the percent loading (w/w) determined by TGA. Both neat SIM and composite were previously enclosed in a cellulose membrane SnakeSkin® (cut-off 3500 Da) purchased from Thermo Scientific, allowing for the diffusion of SIM, but posing a barrier to silica particles. To closely mimic physiological conditions, the assays (three replicates) were performed at constant temperature in an incubator shaker (Comecta SA) regulated to 37 °C and 100 rpm.

2.2.10. Molecular Dynamics Simulations

In the present work, Molecular dynamics (MD) simulations were performed using the DL_POLY package [46] to investigate SIM under confinement at the molecular scale. In order to model MCM-41 mesoporous matrices, we have used a fully pre-optimized configuration of vitreous silica provided in [47], in which the porosity was generated according to the procedure developed by Brodka and Zerda [48]. It allowed us to create a straight cylindrical channel of a mean diameter of about 3.5 nm carved in the pre-optimized amorphous silica (see Figure 1). The inner surface silanol density of about 7.5 OH nm^{-2} agrees with hydroxyl coverage in real highly hydrated silicate surfaces [49]. A set of 46 SIM molecules are confined in this straight cylindrical channel (see Figure 1), very similar to previous studies made on confined glycerol [50].

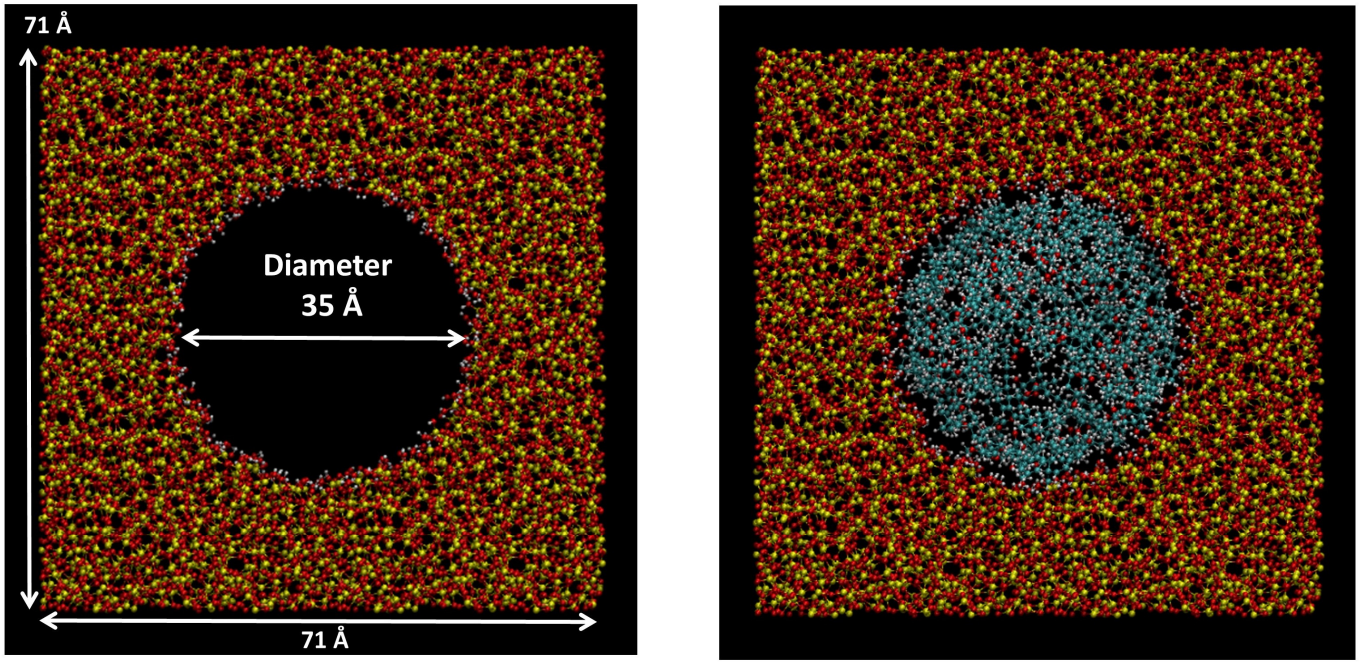

Figure 1. Snapshot of the empty cylindrical channel carved in a pre-optimized rectangular parallelepiped matrix (71 Å × 71 Å × 36 Å) of amorphous silica (**left**) and filled with SIM molecules (**right**). The channel is completely filled with 46 SIM molecules corresponding to the density of SIM in the channel of about 0.94 g cm^{-3}.

MD simulations were performed with a time step of 1 fs using periodic boundary conditions. We have used a semi-rigid model for the silica confinement matrix in which the position of silicon and oxygen atoms were fixed while the silanol hydrogens were allowed to rotate about the Si-O bond axis. In order to compute intra- and inter-molecular interactions, we have employed the all-atom OPLS force field [51] for SIM and the force field developed in [47,48] for silica. Van der Waals and electrostatic interactions between SIM and silica are computed using the Lorentz–Berthelot mixing rules, similar to previous studies [50]. The damped shifted method developed by Wolf was used to calculate coulombic interactions with the same cut-off radius of 10 Å used for both van der Waals.

All simulations of confined SIM were performed in the NVT ensemble (constant number of particles N, volume V, and temperature T). The Nosé-Hoover thermostat relaxation time has been chosen as 0.2 ps. First, one MD simulation of confined SIM has been performed at the temperature T = 600 K. At this high temperature, the system can be considered fully equilibrated over the duration of the MD simulation (150 ns). The diffusive regime is reached, and the time-dependent dipolar correlation function can be extracted. Second, in order to explore a lower and more realistic temperature, the confined SIM system has been rapidly cooled from 600 K to 300 K. This cooling procedure has been performed from ten different configurations obtained at T = 600 K over the MD simulation run. Then, ten independent MD simulations have been thus performed at T = 300 K based on the different states obtained after the repeated cooling processes. At T = 300 K, the system cannot be fully equilibrated, the diffusive regime is not reached, and the time-dependent dipolar correlation function cannot be extracted. However, this procedure involving multiple quenches allows us to obtain some insights into the possible structural organization of the liquid. Positions and dipole orientations of the SIM molecules can be extracted and averaged over the ten MD simulation runs in order to improve statistics.

The individual molecular dipole moments of SIM molecules have been calculated from the expression: $\vec{\mu}(t) = \sum_{\alpha} q_{\alpha} \vec{r}_{\alpha}(t)$ where q_{α} and $\vec{r}_{\alpha}(t)$ are the fixed charge localized on atom α and its position at time t, respectively. We have used a non-polarizable force-field, so fixed charges q_{α} are considered, which are directly taken from the OPLS force field [51]. The dipole moments of SIM molecules have been computed at the different investigated temperatures to obtain all dipolar properties of the system.

3. Results and Discussion

3.1. Textural Analysis

Figure 2a shows the obtained N_2 adsorption (open symbols)-desorption (filled symbols) isotherms for the unloaded (grey curve) and loaded (blue curve) matrices. Unloaded MCM-41 presents a reversible type IV isotherm, as typically found for well-defined parallel mesoporous structures [52], exhibiting an inflection above ($P/P_0 > 0.9$) due to the filling of interparticle porosities or voids. The obtained textural parameters with the Brunauer–Emmett–Teller (BET) method (specific surface area, total pore volume, and average pore diameter determined from BJH desorption branch (Figure 2b), are summarized in Table 1. After loading, the respective isotherm is highly modified revealing negligible nitrogen uptake similar to what is characteristic of a non-porous material with the specific surface area dramatically decreased (Table 1).

The type of isotherm for the loaded matrix is similar to the one found for other drugs loaded in mesoporous silica matrices, in which the filled pores are occluded in respect to N_2 adsorption [53–55]. Since for the here studied composite, the average pore dimensions of MCM-41 (diameter ~3.5 nm) are larger than the molecular size of a SIM molecule (1.14×0.87 nm^2; see inset in Figure 2b), which allows the drug to enter the pores, and therefore, the observed N_2 pore occlusion is not caused by size exclusion (sieving [56,57]).

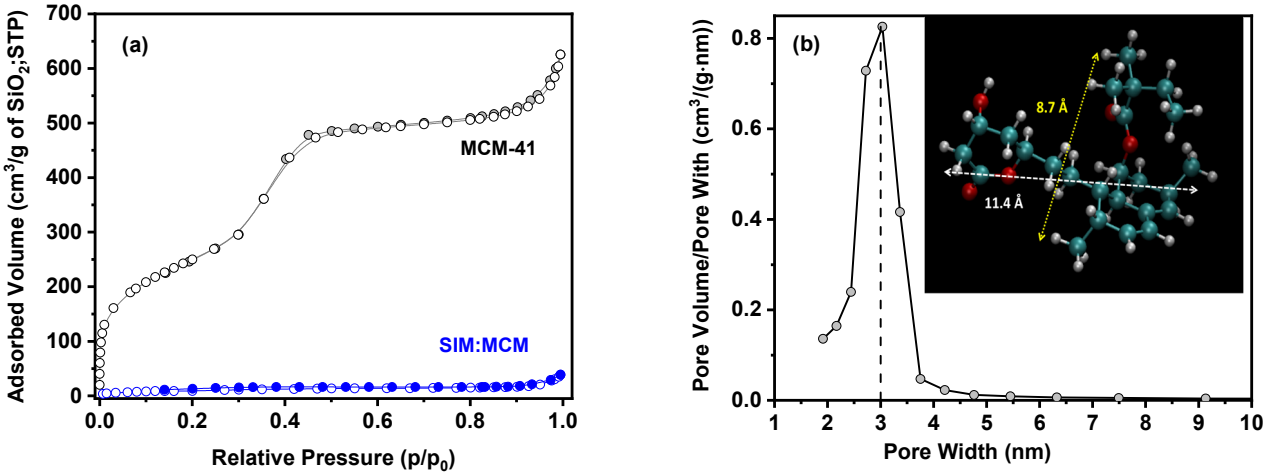

Figure 2. (**a**) Nitrogen adsorption/desorption isotherm for simvastatin loaded MCM-41 (blue circles); unloaded MCM-41 is included for comparison: open circles adsorption; filled circles, desorption branch. (**b**) Pore size distribution for the unloaded matrix (desorption branch), centered at 3 nm. The inset depicts SIM molecular structure and respective dimensions as obtained from Molecular Dynamics simulations.

Table 1. Textural (BET) properties of the unloaded and loaded mesoporous silica matrix, respectively, MCM-41 and SIM:MCM.

Material	Surface Area ($m^2\ g^{-1}$)	Total Pore Volume ($cm^3\ g^{-1}$)	Pore Diameter (nm)
MCM-41	927.3	0.84	3.0 [(a)]; 3.5 [(b)]
SIM:MCM	34.73	n.a. [(c)]	n.a. [(c)]

[(a)] Taken from the maximum peak value of the pore size distribution determined by the BJH desorption branch. [(b)] Average value is determined by the BJH desorption branch. [(c)] Not determined due to the absence of accessible sites for nitrogen adsorption.

3.2. Thermogravimetric Analysis (TGA)

Thermogravimetric analysis was used to evaluate the resistance to thermal degradation of SIM when loaded in MCM-41 and simultaneously to determine the amount of drug loaded in the silica matrix. As will be shown in next section, SIM exists in the amorphous state in the composite (designated hereafter as SIM:MCM); thus, the monitoring of decomposition, besides the neat crystalline SIM, was compared with a previously amorphized sample obtained by cooling from melt (first heating run of the neat crystal up to 170 °C). All samples were submitted to heating from 22.5 °C to 550 °C at a rate of 5 °C min^{-1}. Figure 3a shows the respective weight curves, including the one obtained for the unloaded matrix. Figure 3b shows the derivative plots for neat SIM and loaded matrix.

As a first observation, neat SIM decomposes according to a single step with an onset near 200 °C, and no significant differences occur between crystalline and amorphous samples. On the other side, the TGA curve for SIM:MCM follows a multi-step profile, better seen in the derivative plot (Figure 3b), where the different weight loss stages appear as peaks. After an initial rather small weight loss up to 100 °C due to water removal (1.1%), the weight loss of SIM in the composite occurs according to two steps. The onset of the first step is located at 100 °C, being associated with a fraction of less thermal resistant population ~4.2% ($w_{SIM}/w_{composite}$), meaning 12.6% ($w_{SIM}/w_{SIM\ in\ the\ composite}$). It is followed by a major degradation step with onset at 200 °C showing a greater contribution of a molecular population decomposing at higher temperature relative to neat SIM.

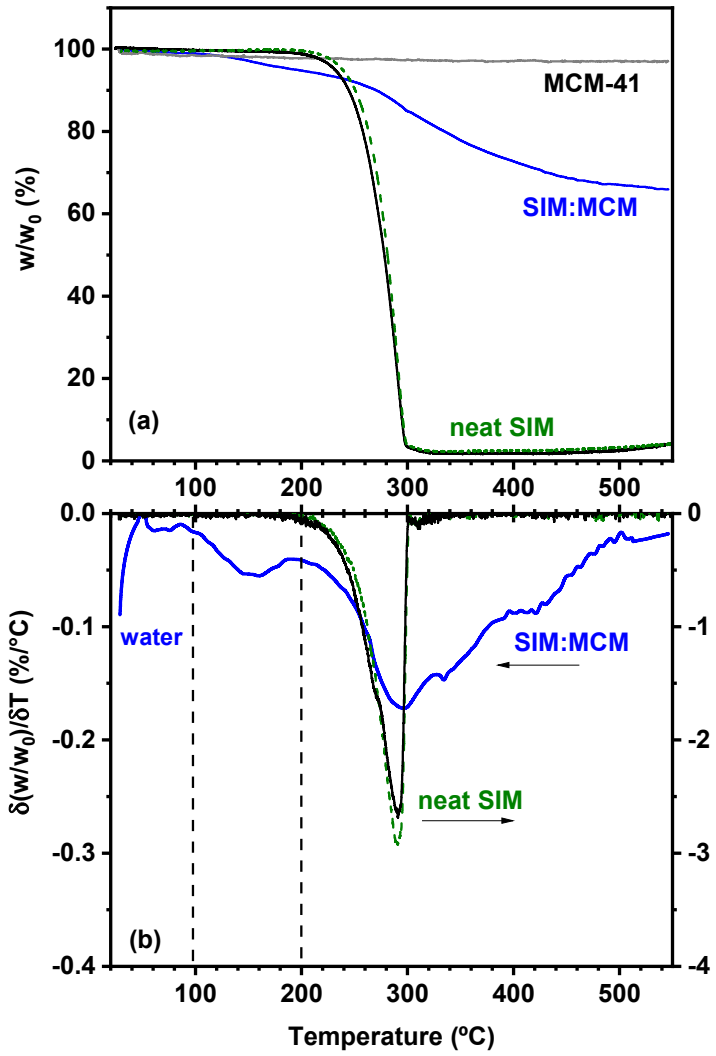

Figure 3. (**a**) Thermogravimetric curves of SIM:MCM (composite containing ~1 mg of simvastatin; blue line), neat crystalline (mass $_{SIM,Crys}$ = 0.9790 mg; black solid line), neat amorphous (mass $_{SIM,Amph}$ = 0.9500 mg; olive dashed line) simvastatin, and unloaded MCM-41 silica matrix (grey line) taken at a heating rate of 5 °C min^{-1}. (**b**) The respective derivative plot for SIM:MCM composite and neat simvastatin (note the different vertical scales).

The unloaded matrix (grey curve in Figure 3a) after dehydration, shows no further weight loss in respect to temperature, as usually found for this type of matrix [35]. From Equation (1), after discounting the mass loss due to dehydration, the SIM loading is determined as 33.0% (w/w) (in agreement with the starting preparation), which, after conversion to volume (Equation (2)), gives a filling of 50.7% (v/v). The BET isotherm obtained for the loaded matrix (Figure 2a), thus corresponding, on average, to partial filling with pores occlusion. Owing to the bulkiness of each SIM molecule and the narrowness of the diameter of the pores, with some contribution of pore sizes below 3 nm (Figure 2b), only a small number of molecules are needed to obstruct the pores opening and filling the smaller pores. Therefore, the complementary information from the TGA and BET analysis indicates a distributed filling of the pores of the SIM:MCM composite.

3.3. Powder X-ray Diffraction Analysis

Figure 4 shows the powder X-ray diffraction pattern at room temperature of SIM:MCM in comparison with neat crystalline simvastatin. The diffractogram of crystalline SIM (black line) is characteristic of form I, assigned to the orthorhombic crystallographic system,

space group, $P2_12_12_1$ [44,58]. It is known that crystalline SIM can exist in three different polymorphs, among which form I is the stable one at room temperature; the other two polymorphs (form II and form III) are only detected at temperatures below room temperature, as first reported by Hušák et al. [59] (synchrotron powder diffraction and ss-NMR studies), and recently by Simões et al. [44]. In the diffractogram of SIM:MCM (blue line in Figure 4), no sharp Bragg peaks are observable, only a broad diffraction halo is detected, which proves that simvastatin is fully amorphous in the SIM:MCM composite.

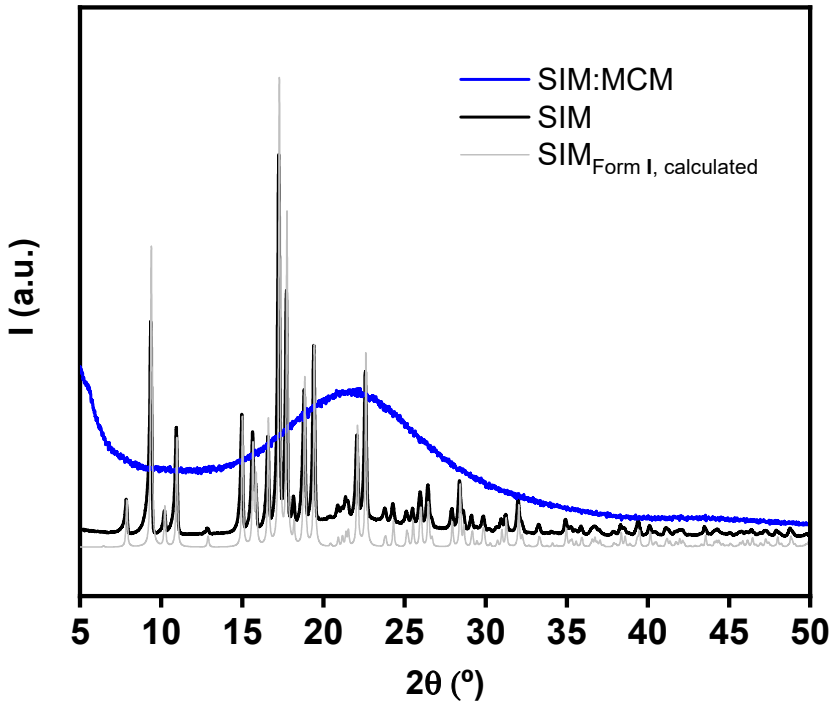

Figure 4. Powder X-ray diffraction patterns, at room temperature, for neat crystalline simvastatin (black line) and SIM:MCM composite (blue line). Data were displaced vertically for better visualization. The calculated diffractogram of SIM crystal Form I (Cambridge Structural Database refcode EJEQAL08) [44] is included for comparison (grey line).

3.4. ^{13}C CP/MAS ssNMR Analysis

The ^{13}C ssNMR spectrum of SIM:MCM is shown in Figure 5. All the ^{13}C resonances are originated by SIM loading as it is possible to notice the absence of ^{13}C chemical shifts in an unloaded MCM sample. The broadness exhibited in the loaded SIM ^{13}C CP/MAS NMR resonances is similar to the spectrum for bulk amorphous SIM provided by Nunes et al., where distinct frequency regions can be found [26]. The complete assignment of ^{13}C resonances of simvastatin has been first reported by Brus and Jegorov [60] (for crystalline form I and solution) and by Hušák et al. [59] (for the three simvastatin polymorphs). The carbonyl groups present a very broad signal between 180–170 ppm, the unsaturated carbons between 150–130 ppm, the C-OR moieties exhibit a broader signal than the previously described for bulk amorphous SIM, with resonances between 90–60 ppm, and the remaining aliphatic carbons appear between 50–10 ppm. The broadness of the carbonyl resonances (C1 and C18; see molecular structure in Scheme 1) supports the existence of a distribution of conformations and the lack of order at shorter distances. Moreover, the observation of broader and downshifted frequency groups is compatible not only with the existence of an amorphous state but also with the establishment of possible SIM-MCM interactions.

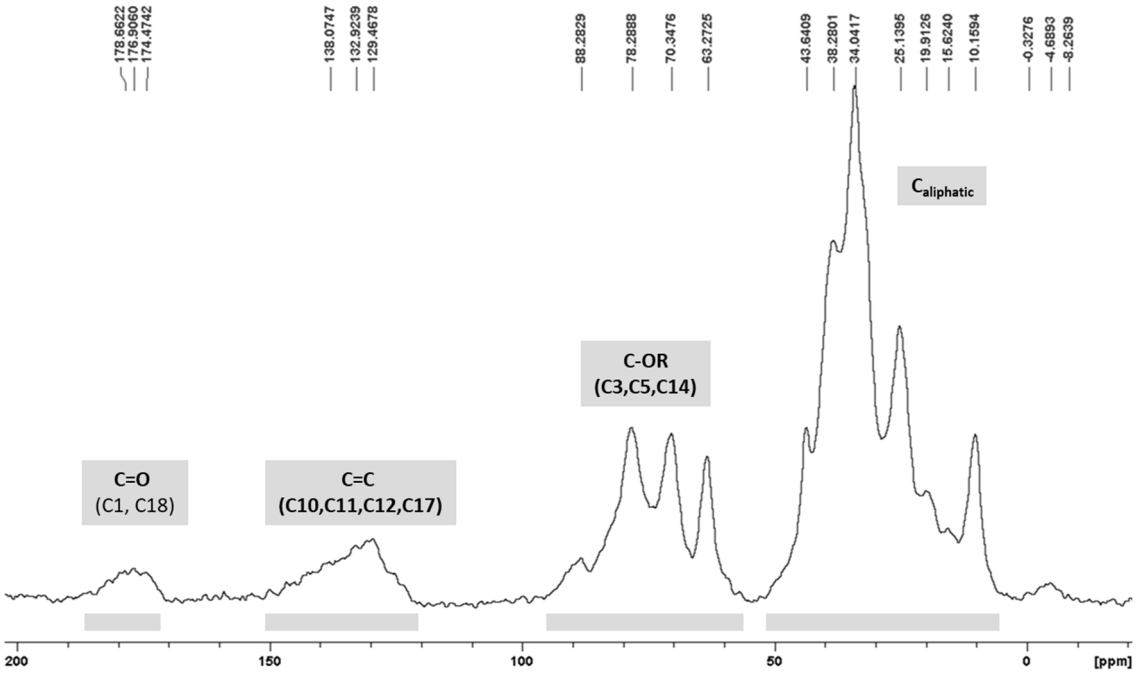

Figure 5. ^{13}C CP/MAS NMR spectrum of SIM:MCM and main groups (see molecular structure in Scheme 1) assignment according to previous works [26,59,60].

3.5. ATR-FTIR Analysis

To get further information about the drug's physical state, ATR-FTIR spectroscopy was used, which also allows for obtaining insights into the SIM intermolecular interactions. The spectrum corresponding to bulk amorphous SIM (see Section 2) was collected in addition to the one of neat crystalline SIM (form I). In this phase, infinite chains along the crystallographic $\vec{b}$ axis are formed due to intermolecular single hydrogen bonds that establish between the hydrogen of the hydroxyl group of the lactone ring (see Scheme 1) of one SIM molecule and the oxygen of carbonyl in the linear butyl ester [44,58] of a second SIM molecule (O3−H···O5). Therefore, the spectroscopic analysis will be focused on the two infrared regions where vibrational modes of O−H (between around 3700 and 3100 cm^{-1}) and C=O (between 1800 and 1600 cm^{-1}) absorb. Free O−H and C=O have characteristic frequencies at approximately 3520 and 1760 cm^{-1}, appearing as sharp lines [61]. All spectra are compared in Figure 6.

The spectrum of neat crystalline SIM in the O−H region is shown in Figure 6a, displaying a sharp band centered at 3547 cm^{-1} due to OH hydrogen-bonded (O3−H···O5) [30]. Upon amorphization, the global spectrum shifts towards a lower wavenumber region, becoming broader (Figure 6b), consistent with what is reported in the literature for the bulk amorphous SIM [27,28,30] due to its less organized structure, evidencing that no free OH groups exist, which would give rise to infrared signals at higher wavenumbers. Therefore, it can be concluded that in the amorphous form, the hydroxyl groups of the lactone ring of all SIM molecules are interacting via hydrogen bonding (HB). This HB interaction of an OH group of a SIM molecule can be established with another OH group (O3−H···O3−H) and/or with the carbonyl group of the ester tail (O3−H···O5) and/or of the lactone ring (O3−H···O2) of a second SIM molecule; see SIM chemical structure and atoms numbering in Scheme 1.

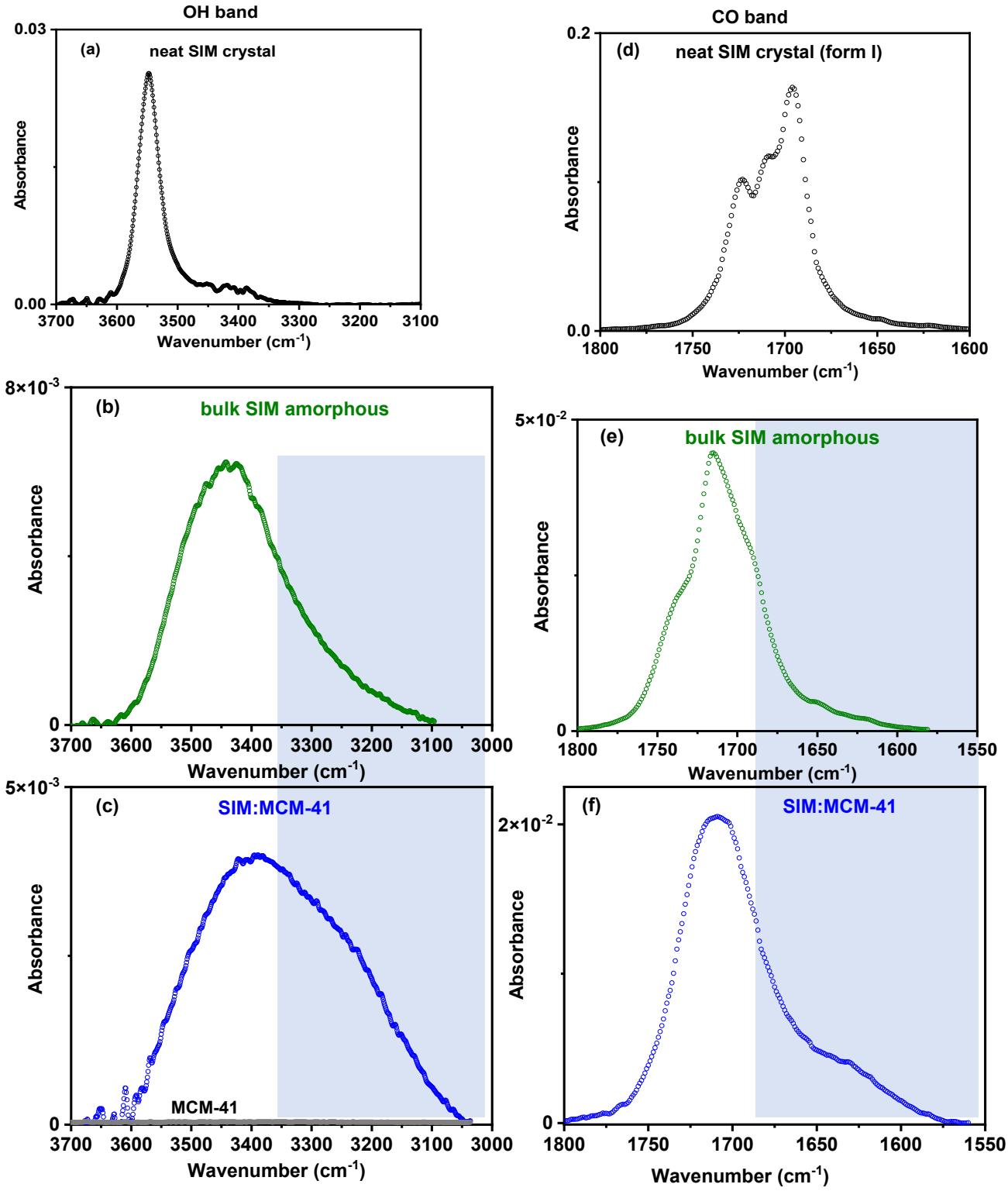

Figure 6. ATR-FTIR spectra at room temperature in the hydroxyl (OH) band (left-hand panels) and carbonyl (CO) band region (right-hand panels) of neat simvastatin (crystal form I and bulk amorphous, respectively, panels (**a**,**b**) and (**d**,**e**)) and SIM:MCM composite (panels (**c**,**f**)).

The profile of the O−H band of SIM incorporated in MCM-41 (Figure 6c) clearly shows no sign of crystalline phase and differentiates from the one of bulk amorphous SIM, having an additional contribution in the low wavenumber region highlighted by the shadowed area. This additional contribution acts as a clear indication that hydrogen bond

interactions between the OH groups of SIM molecules and the silanol (Si-OH) pore wall groups exist. Due to their location at even lower wavenumbers, it is possible to conclude that these guest–host interactions are stronger than those between SIM molecules. Note that the modification of the O−H band comes neither from the matrix itself nor from water vibrations. In fact, the unloaded MCM-41 spectrum is included in Figure 6c (grey line), for which the water content is similar to that of the composite (1.6%(w/w)), being clear that it has a negligible influence on the composite infrared spectrum.

The infrared spectrum of neat crystalline simvastatin in the carbonyl stretching region shows a structured band (Figure 6d) that can be deconvoluted in three contributions (1725, 1710, and 1695.4 cm^{-1}). Details on deconvolution and bands assignment are given in the Appendix A (Figure A1). The band at 1695.4 cm^{-1} is assigned to the stretching of hydrogen-bonded carbonyl in the butyl ester tail, $C{=}O5_{ester,HB}$ (1695 cm^{-1} [29]/1693.5 cm^{-1} [30]) which ensures the infinite one-dimensional chain along the crystallographic $\vec{b}$ axis: O3−H···O5 [44,58]. The remaining two bands, that were also identified in the literature (1720 and 1708 cm^{-1}) [29], are assigned to stretching modes of the lactone carbonyl group, $C{=}O2_{lact}$, which is involved in weak HB interactions, C9−H···O2 and C2−H···O2, ensuring the 2D and 3D molecular packing in crystalline SIM [44]. In bulk amorphous SIM, the 1750–1500 cm^{-1} spectral region (Figure 6e) is modified according to what is already reported in the literature [28–30]. The shift to higher wavenumbers of the global band suggests that, at least partially, carbonyl groups of the ester butyl tail become weakly or free HB in the amorphous state.

In the SIM:MCM composite (Figure 6f), the global band of carbonyl absorption becomes less structured, being centered at a slightly lower wavenumber than that of bulk amorphous SIM, with an additional low wavenumber contribution, highlighted by the shadowed area. The appearance of a low wavenumber contribution indicates that SIM molecules are strongly interacting with the silanol groups of the MCM-41 pore wall via the carbonyl groups (O5···H−O−Si and/or O2···H−O−Si) in addition to the hydroxyl-silanol interactions revealed by the analysis of the O−H vibration band (Figure 6c).

ATR-FTIR analysis of the SIM:MCM composite clearly indicates the existence of a fraction of simvastatin molecules strongly interacting with the inner walls of MCM-41 pores, consistent with the high thermal resistance population evidenced by TGA analysis.

3.6. Differential Scanning Calorimetry (DSC) Analysis

PXRD, ssNMR, and ATR-FTIR analyses at room temperature gave evidence that SIM loaded in MCM-41 is in an amorphous state. To better understand its physical state and thermal behavior, calorimetric measurements were performed in a wide temperature range for SIM:MCM composite in comparison with neat crystalline SIM and bulk amorphous SIM.

Figure 7a depicts the DSC curves collected in the first heating at 10 °C min^{-1} for neat crystalline SIM (black line) and SIM:MCM composite (blue line). The sharp melting endotherm centered at T_m = 141 °C ($T_{m,onset}$ = 140 °C) with an associated enthalpy of ΔH_m = 74.14 J g^{-1} (31.0 kJ mol^{-1}) is characteristic of Form I, in close agreement with which is reported in the literature [26,62]. The absence of a melting peak in the DSC curve collected in the first heating run for SIM:MCM (blue line in Figure 7a) confirms that no crystalline SIM exists in the composite, in agreement with the spectroscopic analyses (ATR-FTIR and ssNMR) and PXRD, in which only the amorphous halo is detected. The absence of melting indicates that no drug exists outside the pores, contrary to what was observed for a different batch prepared with a higher SIM/MCM weight ratio (see additional DSC results in Appendix A, Figure A2).

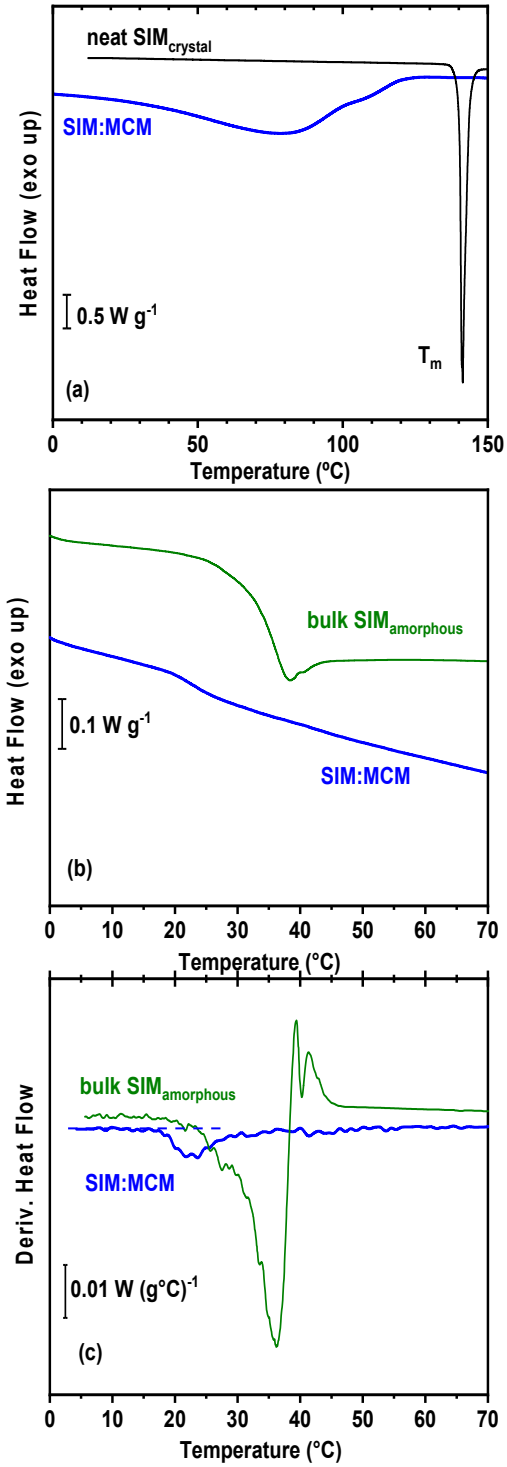

Figure 7. (**a**) DSC curves of SIM:MCM (taking in account the weight % of SIM+water in the composite) and neat SIM crystal (form I) during heating at 10 °C min^{-1}. (**b**) DSC curves of SIM:MCM (taking in account the weight % of SIM in the composite) and bulk SIM amorphous during heating at 30 °C min^{-1} (after previous cooling at 30 °C min^{-1} of the dried composite and melt neat SIM). (**c**) Temperature derivative of heat flow curves shown in (**b**).

In the DSC curve (Figure 7a), a broad endotherm due to water removal is detected, making it difficult to observe, in this first run, a heat capacity step associated with the glass transition of amorphous SIM in the composite. From the weight loss registered at the end of the DSC measurement, a 2.0% (w/w) was determined for the water amount

in the composite, in close agreement with TGA quantification, despite the long period of time between the different analyses. This low tendency of SIM:MCM composite for water uptake is compatible with the picture of SIM molecules adsorbed at the pores entrance, impairing the incoming of water molecules, which occurs for nitrogen in the BET assay shown in Figure 2a.

After water evaporation, a low intense discontinuity associated with the glass transition is detected in the following curve at 10 °C min^{-1} (not shown). To increase the steepness of the heat flow discontinuity at the glass transition temperature (T_g), the DSC curve was acquired with a higher heating rate (30 °C min^{-1}), better revealing the glass transition step (blue curve in Figure 7b). The respective onset is located at a temperature inferior to the one of bulk amorphous SIM, carried out at the same heating rate (blue vs. green curve in Figure 7b). The glass transition becomes also evident in a heat flow derivative representation against temperature, where it emerges as a downward peak; this is shown in Figure 7c for both composite and bulk SIM. The obtained profile of confined SIM points to the inexistence of a bulk amorphous fraction outside the pores, contrary to what was observed for a different batch prepared with a higher SIM/MCM ratio (Figure A2 in Appendix A). A T_g decrease of ~15 degrees relative to bulk amorphous SIM is observed, as seen by the difference between the peak's minima in the derivative plot. Trying to quantify this highly mobile population, the heat capacity variation at T_g, $\Delta C_{p,SIM:MCM}$ was compared with the respective heat capacity of bulk SIM, $\Delta C_{p,SIM}$ after correction for the SIM mass in the dehydrated composite and taking into account the loading degree (33% (*w*/*w*)). The obtained ratio ($\Delta C_{p,SIM:MCM}/\Delta C_{p,SIM} \times 100$) gives ~13.7% of the total SIM population in the SIM:MCM composite, corresponding to 4.5% (*w*/*w*) in relation to the total composite mass, in good agreement with the 4.2% (*w*/*w*) less thermal resistant SIM fraction as quantified by TGA.

The onset of the glass transition at lower temperatures relative to bulk SIM, and the absence of an enthalpy overshoot, which appears superimposed on the glass transition heat flux step for bulk amorphous SIM (positive peak in the bulk SIM derivative plot shown in Figure 7c), are features also found for ibuprofen incorporated with an analogous filling in a similar MCM-41 matrix (average pore diameter 3.5 nm) [35]. This was interpreted as a consequence of confinement effects [63,64] manifesting when the pore dimensions of the host matrix interfere with the drug cooperative length scale, being originated by an accelerated pore-core population. In the ibuprofen-loaded MCM-41, the glass transition is rather broadened compared with the bulk drug, extending to temperatures above the bulk one. This is due to a population inside pores that gradually distributes from the accelerated molecules in the pore core, with no interactions with the silica surface, to a high-T hindered population associated with pore-wall adsorbed ibuprofen molecules, however, keeping some limited mobility. Differently, in SIM:MCM composite, only the decreased glass transition contribution is clearly found with a lack of a calorimetric signature of the remaining loaded population whose existence has been clearly demonstrated by the thermogravimetric analysis. Therefore, the non-existence of a change in heat capacity at high temperatures indicates a highly constrained molecular population impeded in terms of its ability to undergo configurational rearrangements as a consequence of strong adsorption on the silica matrix. This was evidenced by ATR-FTIR, and it is coherent with an extended high thermally resistant fraction found by TGA.

To get further insight in the dynamical behavior of SIM confined in the composite, measurements by dielectric relaxation spectroscopy were carried out and compared with bulk amorphous SIM.

3.7. Dielectric Analysis

Dielectric relaxation spectra of SIM:MCM were collected isothermally in the temperature range from −95 °C to 165 °C after a prior run carried out up to 100 °C to assure water release (see details in Appendix A, Figure A3). Note that the MCM-41 matrix itself (dried) does not contribute to the dielectric spectrum of the composite [35]. The comparison of the

dielectric response of loaded simvastatin (after dehydration) with bulk amorphous SIM is shown in Figure 8.

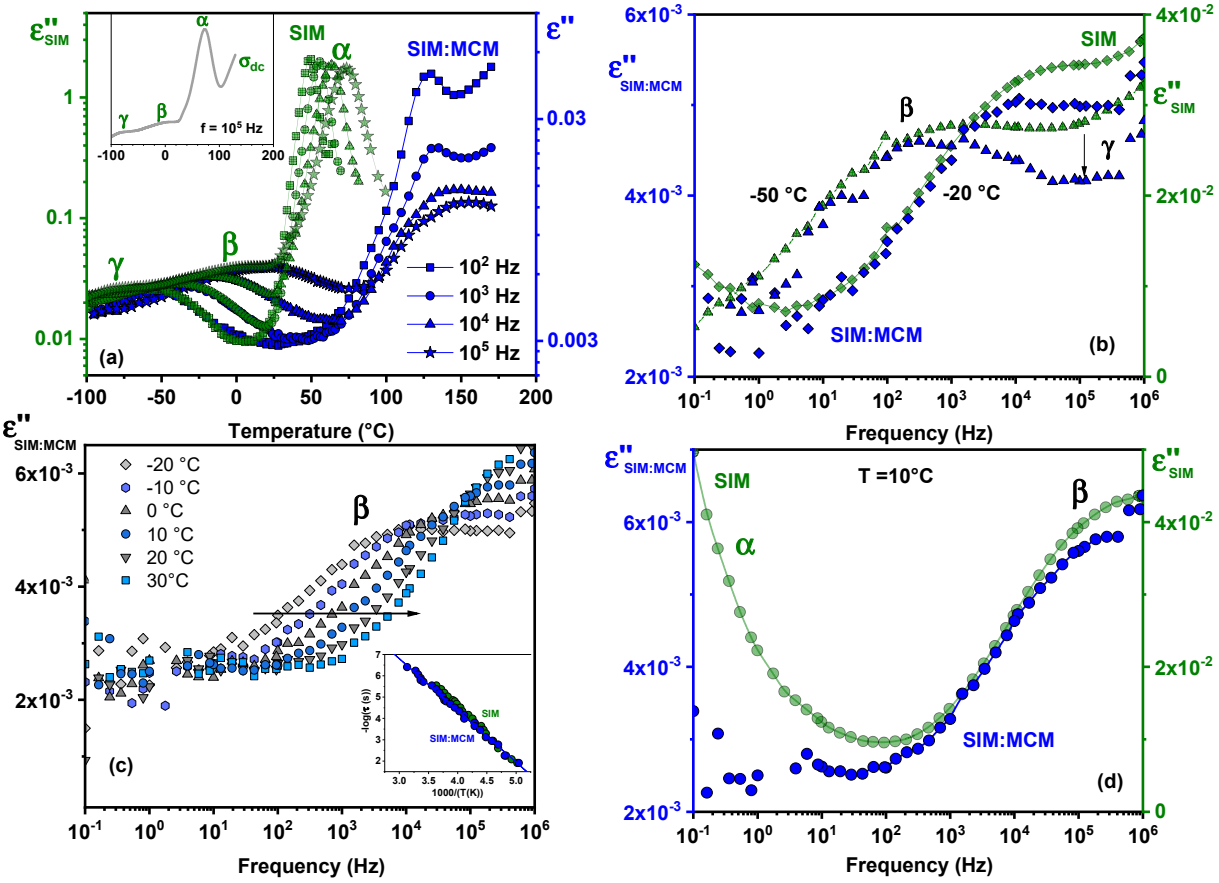

Figure 8. (**a**) Comparison of dehydrated SIM:MCM (blue symbols; right-hand axis) with bulk amorphous SIM (olive symbols; left-hand axis) in terms of the imaginary part, ε''(T), at four frequencies (see caption inside figure). In the inset, the ε''(T)-trace at 10^5 Hz for bulk SIM, where the different dielectric processes, γ, β, α, and conductivity (σ_{dc}) are identified; the conductivity tail of bulk SIM was removed from the ε''(T)-trace in the main figure. ε''(f) isothermal plots of SIM:MCM: (**b**) compared with bulk SIM at −50 °C and −20 °C; (**c**) between −20 °C and 30 °C. The inset displays the temperature evolution of β relaxation times (−log(τ) vs. 1/T) of SIM in the composite (blue circles) and bulk SIM (olive circles); (**d**) compared with bulk SIM at 10 °C.

Figure 8a depicts the isochronal plots of the imaginary component of the complex permittivity (ε''(T)) at four different frequencies, between 10^2 and 10^5 Hz. Bulk amorphous SIM presents two relaxation processes associated with local mobility (named γ and β in increasing order of temperature) at the lowest temperatures, and, above ~25 °C, the signature of the high-intense process associated with the dynamic glass transition (α); at the highest temperatures, the spectra are influenced by direct current conductivity (σ_{dc}), removed from main figure for clarity, but included in the inset. The detected processes agree with the literature reports [26,34]. As the main dipolar moieties, in a SIM molecule, are the hydroxyl and ester butyl tail (see Scheme 1), the dielectric secondary relaxation processes are associated with fluctuations of these polar groups as assigned in a joint study by DRS and solid-state nuclear magnetic resonance spectroscopy [26]. The latter technique gives evidence that the polar hydroxyl group is the one presenting the higher resonance frequency. Since the OH group is the more mobile one, its reorientational motions should be associated with the γ-process, the one dielectrically detected at the highest frequencies (faster relaxation rate), which, in an isochronal plot, emerges at the lowest temperatures. While this process is noticed in the ε''(T)-trace of bulk amorphous SIM (inset of Figure 8a),

it is not so clearly seen in the composite being probably highly depleted. As the ATR-FTIR spectra showed, both bulk and loaded SIM have no HB-free OH groups. However, in SIM:MCM composite, a fraction of OH groups are hydrogen bonded to the matrix silanol moieties (low wavenumber region highlighted in Figure 6c) instead of other SIM molecules as occurs in the bulk drug. Therefore, the weak dielectric response of the γ-relaxation (Figure 8c) in SIM:MCM reinforces the infrared analysis, which points to the existence of a fraction of molecules strongly anchored to the pore wall hindering the OH group mobility.

Concerning the β-process, it is clearly noticed in the isochronal plot of SIM:MCM composite (the low-temperature region in Figure 8a), keeping the same location and overall shape as the respective process detected for bulk SIM. The resemblance of the dielectric response is also shown by the isothermal representation at −50 °C and −20 °C (see Figure 8b). Figure 8c presents the spectral temperature evolution in SIM:MCM evidencing that the same temperature increment provokes equal frequency shift in the loss peak of the β-relaxation (this type of change in peak position with temperature is characteristic of a thermally activated process). The inset of Figure 8c depicts the predicted linear dependence against 1/T of the logarithm of the respective relaxation time (τ), estimated from the peak maxima in an isochronal representation (Figure 8a; the maximum temperature of the β-peak in the ε''(T)-trace, T_{max}, is taken for each frequency, f and $\tau = 1/(2\pi f)$). The fitting by the Arrhenius law, $\tau(T) = \tau_\infty \exp(E_a/RT)$ (R (ideal gas constant) = 8.3145 J mol^{-1} K^{-1}), gives an activation energy of 47 kJ mol^{-1} for SIM:MCM, close to the corresponding value in bulk SIM, 52 kJ mol^{-1}, and in good agreement with the values reported in the literature [34]. This Arrhenius temperature dependence is characteristic of local, intramolecular secondary relaxations, which should be attributed to dipolar fluctuations in the ester tail, in line with solid-state NMR observations [26]. The dipolar moieties contributing to the detected β-process in SIM:MCM must correspond to a fraction of the butyl ester groups that are non-interacting with the matrix and, thus, have comparable mobility to the homologous intramolecular process in bulk amorphous SIM. This points to the sensitivity of DRS for probing short-length scale motions in a complex system in which only a small fraction of the sample responds dielectrically.

Figure 8c also evidences the nonappearance of a cooperative bulk-like α-process in the low-frequency tail of the β-relaxation in SIM:MCM, unlike what happens in the bulk SIM, as illustrated in the isotherm at 10 °C shown in Figure 8d. This is in line with what was found by DSC, where no significant heat flux discontinuity associated with a bulk glass transition was detected; instead, a small C_p jump at a lower temperature was found. The latter, in dielectric measurements, should correspond to a weak α_{fast}-relaxation and, therefore, is expected to appear at lower temperatures/higher frequencies relative to the SIM bulk α-process, approaching and probably submerging under the bulk-like β-process. However, no significant change in the shape of the dielectric loss peak of the β-process is observed, as one would expect if such a coupling of relaxation processes of a different nature (intermolecular versus intramolecular, respectively, for the α and β-process) has occurred. Therefore, we can hypothesize that the molecular arrangement of SIM molecules inside the core of the pores leads to a strong decrease or even total cancellation of the global relaxing dipole moment weakening the corresponding α_{fast}-relaxation dielectric response. This feature will be further elucidated by MD simulation studies (Section 3.9).

It is worth mentioning that recrystallization was not observed for loaded SIM, even after 3 years of storage at ambient conditions. This, in addition to the evidence that no recrystallization was observed when SIM:MCM was subjected to thermal treatments (DSC and DRS), can be taken as an indication that the critical nuclei diameter for crystallization is higher than 3.5 nm and, therefore, no driving force exists to trigger crystallization when SIM is confined to such narrow pore size.

Additionally, in the isochronal plot of SIM:MCM composite (Figure 8a), a high-temperature tail emerges that needs clarification. Taking other low molecular weight glass formers loaded in similar matrices as reference [63,65,66], they typically exhibit two high-temperature processes: (I) a surface one due to the relaxation of weakly adsorbed

molecules at the inner pore wall, which are still mobile but with reduced mobility compared to non-adsorbed molecules; and (II) an interfacial polarization (Maxwell–Wagner–Sillars (MWS) process [67]), characteristic of disordered inhomogeneous media where dielectrically different material coexists. While process (I) gives a high temperature glass transition signature in DSC, the MWS process has no calorimetric response. Given that in SIM:MCM composite, no signal is clearly distinguished by the calorimetric analysis, other than the low-T glass transition, as already commented, it seems reasonable to attribute the dielectric peak, emerging at high-temperatures, to interfacial polarization building up at the guest–host interfaces. Furthermore, also some SIM evaporation could contribute, above 100 °C, leading to an apparent frequency-independent peak in the ε''-trace at ~130 °C. This possibility just gains relevance in DRS isothermal spectral acquisition, carried out here in steps of 2–5 °C, with an equivalent heating rate between 0.4 °C and 0.6 °C min^{-1} (much lower than the heating rate practiced in the DSC analysis), which may give time for evaporation of a small SIM fraction.

The non-detection of a dielectric and calorimetric high-T surface process, indicating that the associated population of SIM molecules are dynamically rigid (in the temperature range explored) provides further evidence that these molecules interact strongly with the host surface, corroborating the information from infrared and thermogravimetry analyses.

3.8. In Vitro Drug Release Studies

Simvastatin release from the MCM carrier was monitored by UV-Vis spectroscopy in a phosphate-buffered solution (pH = 6.8) at 37 °C and 100 rpm, to mimic intestinal fluid; crystalline simvastatin's dissolution was followed under the same conditions. The obtained profiles are shown in Figure 9, after normalization by the total amount of SIM used in the respective assay: 2.9 mg/200 mL solution for neat crystalline SIM and 8.5 mg composite/200 mL solution (corresponding to 2.8 mg of amorphous SIM loaded in MCM as estimated from the TGA analysis), after averaging over three trials.

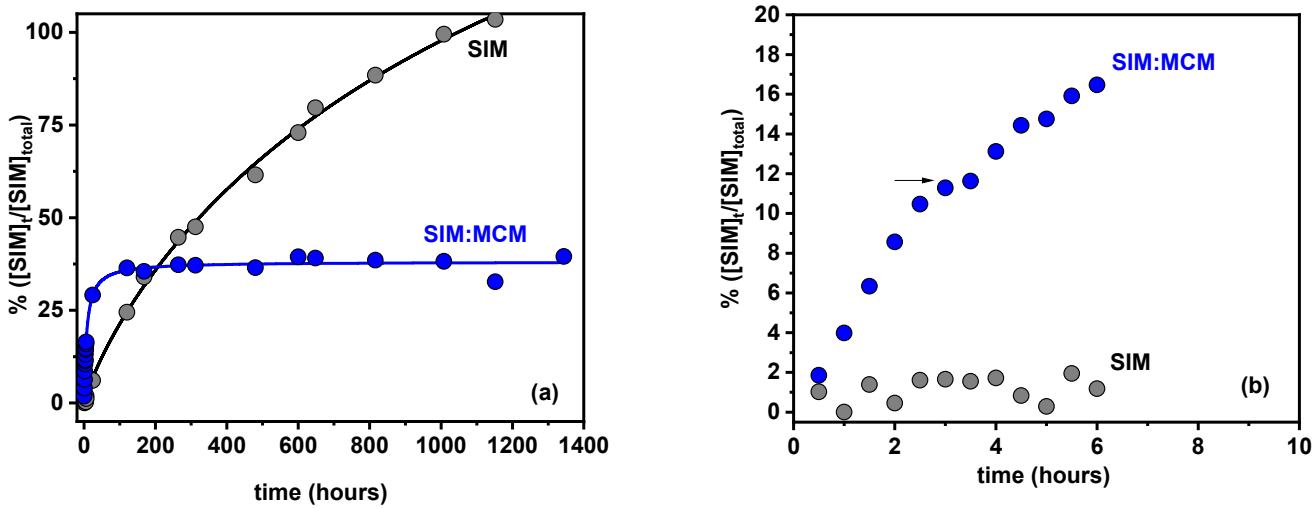

Figure 9. Simvastatin´s dissolution (grey circles) and release from MCM (blue circles) normalized for the total quantity used in the trial (averaged over three trials; error bars are of the order of the data point symbol): (**a**) As monitored for 56 days (solid lines are a guide for the eyes). (**b**) scale up of the first 10 h evidencing the superior releasing rate of loaded amorphous SIM compared with the neat crystalline drug dissolution.

As displayed in Figure 9a, a completely different profile was obtained for the SIM release from MCM carrier (blue circles) as compared with the crystalline drug dissolution (grey circles). Indeed, an almost insignificant dissolution of the latter occurs in the first 6 h, as scaled up in Figure 9b, and only after 30 h does it starts to progressively dissolve, attaining completion after 56 days (1344 h). This behavior reflects the very low dissolution

rate of such poorly water-soluble drug. It is important to note that trials were conducted at ~13 mg L^{-1} of SIM in either crystalline state (dissolution assays) and amorphous in SIM:MCM (release assays), a concentration lying below the solubility limit of crystalline SIM, 24.4 mg L^{-1} as determined under the same pH and temperature conditions [8].

By other side, in the same initial period, a significant amount of SIM is released from the MCM carrier, evidencing how drug amorphization leads to the enhancement of dissolution rate relative to crystalline SIM. A ~12% $SIM_{released}/SIM_{total}$ fraction is delivered in the first 3 h from the SIM:MCM composite, as denoted by the first stage in the release profile (see Figure 9b). This amount compares to the less thermal-resistant population quantified by TGA (conversion from 4.2% $w/w_{composite}$ to 12.6% w/w_{SIM}) and to the heat capacity step registered in the DSC curve (13.7% w/w_{SIM}). Therefore, the first fraction released should correspond to the delivery of SIM molecules with increased mobility (low T_g) as provided by DSC and diffusing from the center of the pores. Subsequently, some adsorbed molecules, most likely not strongly interacting with the pore walls, are released. Nevertheless, the composite SIM:MCM never attains full release, the maximum percentage being 39.6% $SIM_{released}/SIM_{total,}$ indicating that a significant fraction of population (~60%) remains trapped inside pores. This is due to the strong attraction of SIM molecules with the host surface, as highlighted in previous sections. Moreover, as will be seen in the next section (molecular dynamics simulation studies), the fact that SIM interacts with the inner pore walls via multiple hydrogen bonds involving the hydroxyl and carbonyl groups of the lactone ring and also the carbonyl of ester tail, leaves a hydrophobic molecular domain facing the center of the pores, an effect that is even more striking for the configuration in which SIM is simultaneously attached to the pore wall at five sites. This hydrophilicity reduction decreases surface wettability, impairing the entrance of the aqueous-releasing media and, consequently, the release of the pore-wall attached drug.

3.9. Molecular Dynamics Simulations

Molecular dynamics (MD) simulation studies (see details in the Methods Section) were performed to investigate the structural and dynamical properties of the SIM molecules inside MCM-41 pores. The simulated pore diameter (Figure 1) is close to the average pore size ~3.5 nm given by BJH desorption branch for the MCM-41 carrier used in the present work, which has a very narrow pore size distribution (see Figure 2b).

Figure 10 shows the radial density function of SIM molecules along the pore radius r, at T = 300 and 600 K. The density profiles were computed by considering the center of mass of SIM molecules. The effects of the confining matrix on the fluid structure are clearly emphasized by the overall profile.

At r > 10 Å, the presence of a broad and intense contribution demonstrates that the molecules organize by forming a clear surface layer due to the interaction of the SIM molecules with the surface. The formation of strong hydrogen bonds between the SIM molecules and the silanol groups on the silica surface is clearly suspected, as displayed in Figure 11. Such a surface-induced layering has already been observed from MD simulations in many systems [50,68]. Interestingly, this intense peak at radius larger than about 10 Å (Figure 10) exhibits two components, which could originate from the large size and non-globular shape of the SIM molecule (see Scheme 1 and inset of Figure 2b) characterized by at least two characteristic dimensions 8.7 Å to 11.4 Å. In Figure 11b, the center of mass of the SIM molecules is closer to the pore surface than in Figure 11a, which could also explain the existence of two components in the broad peak of radial density function at r > 10 Å (Figure 10). It could be noted that the overall shape of the radial density profile (peaks position and maxima intensity) close to the surface r > 10 Å is weakly affected by temperature, suggesting that this surface layer exists at all temperatures. At distances r < 10 Å, the modulation of the radial density is less marked and vary around the expected average density of SIM in the channel (0.94 g cm^{-3}). At T = 600 K, one may notice a bump at r = 6 Å which could indicate the presence of a second layer. At T = 300 K, the presence of multiple visible broad but distinct peaks may reveal a structuration of the liquid as the

temperature is lowered. SIM molecules cannot be thus considered as really bulk-like in the central part of the pore oppositely to the trend observed for smaller molecules, such as water ([50,68,69]), confined in a similar type of mesoporous matrix. This could originate from the large size of the SIM molecule (see inset of Figure 2b) with characteristic dimensions ranging from 8.7 Å to 11.4 Å to be compared to the pore size of 35 Å. Interestingly, the presence of a clear minimum in the radial density function at a distance close to 10 Å allows us to clearly distinguish one inner zone of the pore (i.e., the central part of the pore or pore volume) at r < 10 Å and one outer zone of the pore close to the surface at r > 10 Å (pore surface). The possibility to clearly distinguish these two zones will be employed in the following.

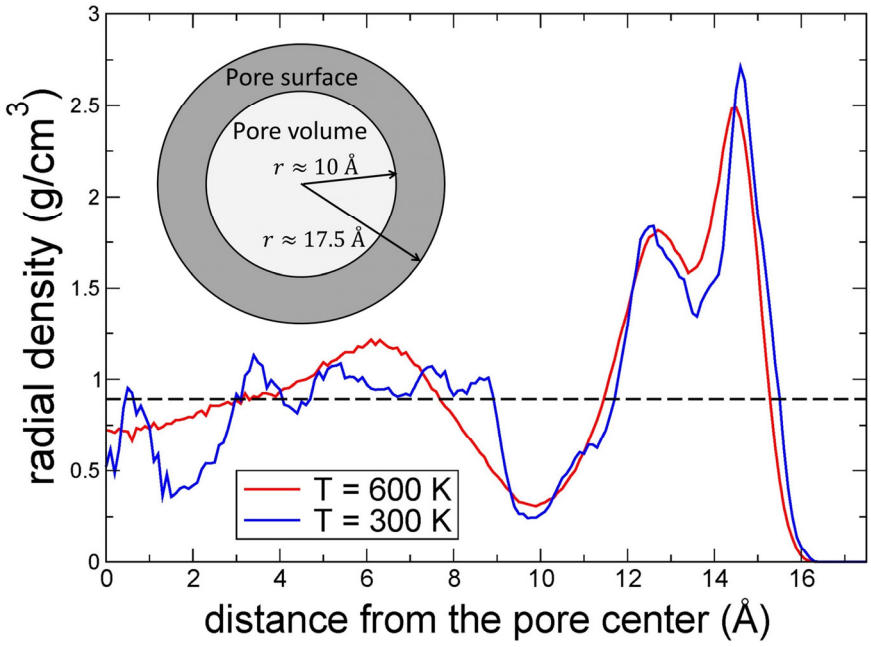

Figure 10. Radial density function of confined SIM at T = 300 and 600 K. The distance r from the pore center is calculated based on the center of mass position of the SIM molecules. Dashed line indicates the expected average density of SIM in the pore (0.94 g cm^{-3}) considering the volume of the pore of cylindrical shape and the number of molecules.

Figure 12 provides some insights of the orientation of the SIM molecules inside the mesopore. It shows the distribution $P(\phi)$ of the angles ϕ of the SIM molecules, for which ϕ is the angle between the dipole moment of the SIM molecules and the vectors normal to the pore surface (see Scheme 2). The function $P(\phi)$ has been computed for the SIM molecules in the pore volume and the pore surface zones and at the two investigated temperatures 300 K and 600 K. Interestingly, Figure 12 reveals that dipoles are not randomly distributed inside the mesopore but show a preferential orientation ($\phi \approx 0$). Dipole moments are thus preferentially pointing toward the pore surface. This behavior is consistent with molecules participating in some H-bonds with SIM interfacial oxygens and hydrogen atoms belonging to the pore itself (see Figure 11). This trend is very marked for the dipoles close to the pore surface, i.e., for molecules in direct interaction with the surface, but it is even also observed for the dipoles in the pore volume, although the effect is less important. Actually, it confirms that SIM molecules are not bulk-like, even in the central part of the mesopore. The alignment of the SIM dipoles toward the surface also seems to amplify upon decreasing the temperature, as shown by the increase in the $P(\phi \approx 0)$ intensity from 600 K to 300 K. This strong preferred orientation of SIM dipoles in the pore (especially in the vicinity of the surface) which differs to the bulk phase where SIM dipoles do not exhibit any preferential orientation may have a strong consequence for all dielectric properties

observed in confinement. One may thus expect a strong decrease in the dielectric strength because dipoles cancel each other's due to their radial orientation.

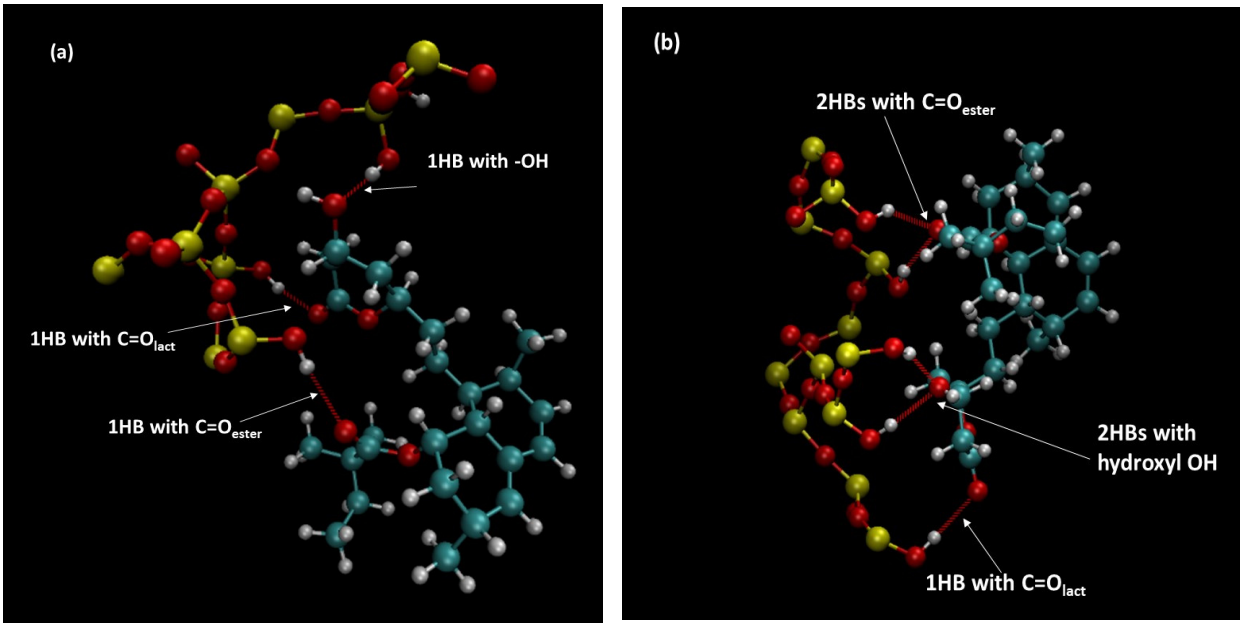

Figure 11. Zoom of the simulation cell obtained by MD simulations of simvastatin confined in a cylindrical pore of 3.5 nm diameter that mimics MCM-41 mesoporous materials, illustrating the interaction of one simvastatin with the silanol groups of the MCM matrix through (**a**) three hydrogen bonds and (**b**) five hydrogen bonds identified by the white arrows. The snapshots illustrate well that the surface-anchored SIM molecules adopt a conformation that leaves a hydrophobic part towards the center of the pore.

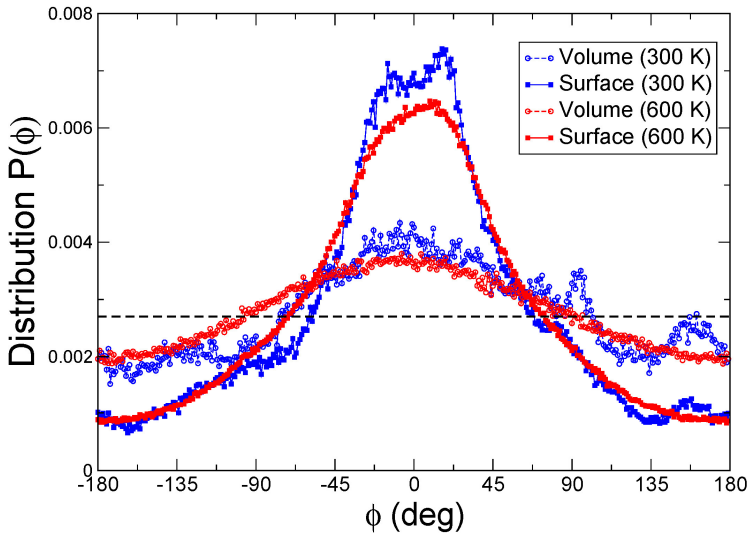

Figure 12. Distribution $P(\phi)$ of the angles ϕ of the SIM molecules present in the pore volume or the pore surface at T = 300 and 600 K. ϕ corresponds to the angle formed between the SIM dipole moments $\vec{\mu}$ and the vector perpendicular to the pore surface (See Scheme 2). $\phi = 0$ corresponds to a situation where the dipole moment of the SIM molecule is radial, i.e., pointing along the direction perpendicular to the pore surface. At $\phi = \pm 180°$, the dipole moment of the SIM molecule is parallel or antiparallel to the pore surface. The horizontal dashed line indicates the expected value for a distribution of randomly orientated dipoles as expected in the bulk.

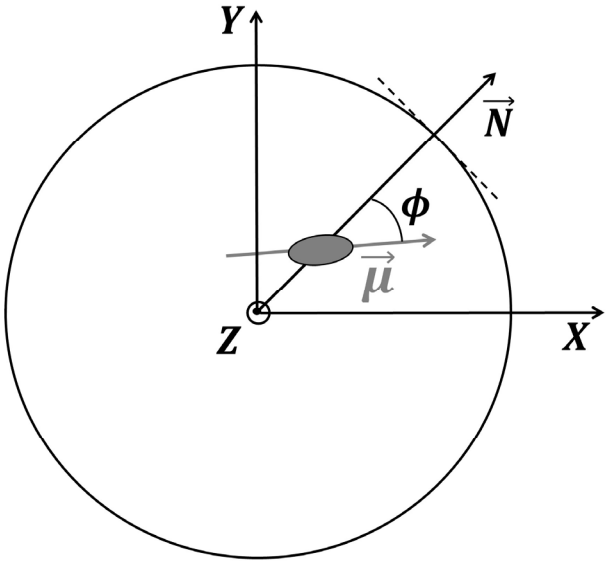

Scheme 2. Schematic representation of the plane (OXY) perpendicular to the pore cylindrical channel. The direction OZ is orientated along the channel. ϕ represents the angle between the SIM dipole moment $\vec{\mu}$ and the vector normal to the pore surface $\vec{N}$. $\vec{N}$ is connecting the pore center and the center of mass of the SIM molecule.

These results of MD simulations clearly explain the non-detection by dielectric relaxation spectroscopy of an α_{fast} process associated with the SIM molecular population with accelerated mobility in the center of the pores, highlighted by a jump in heat capacity in the DSC curve of the confined simvastatin, at lower temperatures than bulk SIM (see Figure 7b).

4. Conclusions

Simvastatin, a lowering high-cholesterol drug, was loaded onto MCM-41 mesoporous silica (~3.5 nm average pore diameter) as an approach to stabilize it in the amorphous state and enhance its dissolution in an aqueous medium. To access the physical state of the loaded drug and its in-pore distribution, a variety of experimental techniques was used (PXRD, ssNMR, and ATR-FTIR), showing that SIM is fully amorphous upon loading; however, it is unevenly distributed inside pores. Molecular Dynamics simulations provide evidence for this pore diameter, that most SIM molecules tend to accumulate near the inner pore wall, forming a surface layer anchored at multiple sites through up to five HBs. This is in accordance with both infrared and thermogravimetric analysis, which revealed strong guest–host interactions and a high thermal-resistant population, respectively. Moreover, the multiple binding sites turn the anchored molecules dynamically rigid and, therefore, lacking a calorimetric signature and a resolved response in dielectric relaxation spectroscopy.

MD simulations also predicted a pore core molecular fraction spatially limited to a pore radius ~1 nm that adopts preferential radial orientation of dipoles distinct from bulklike SIM. This is consistent with the detection of a calorimetric glass transition with an onset decreased by around 15 degrees relative to bulk amorphous SIM and considered a manifestation of true confinement effects. Failure to detect a corresponding α_{fast} dielectric process is due to the cancellation of the overall dipole moment. However, intramolecular motions were able to be detected originating: (i) a γ -process assigned to dipolar reorientations of the lactone hydroxyl groups, and (ii) a β relaxation with better resolution, attributed to rearrangements of the carbonyl carrying ester tail.

The pore-core mobile fraction, first released from the MCM carrier, exhibits a highly enhanced delivery rate compared to neat crystalline SIM dissolution. Furthermore, the narrowness of the pore size prevents drug recrystallization and, therefore, incorporation in

MCM proved to be a suitable strategy to improve the release rate and allow the long-term stabilization of SIM in the amorphous state (at least three years after incorporation).

The thorough investigation of SIM:MCM by complementary techniques and methods carried out in this work allowed the fundamental understanding of the target material relevant to the future design of controlled drug delivery systems.

Author Contributions: Conceptualization, M.D., N.T.C. and F.A.; methodology, T.C., I.M., J.C.S., M.C.C., F.D. and M.D.; software, F.A.; validation, F.A.; formal analysis: T.C., M.C.C., M.T.V. and N.T.C.; investigation, T.C., I.M., F.D., J.C.S. and M.C.C.; resources, M.D., I.M.F. and N.T.C.; writing—original draft T.C., N.T.C., M.T.V. and M.D.; writing—review and editing F.A., I.M., M.C.C., M.D., M.T.V. and N.T.C.; visualization, N.T.C. and F.A.; Supervision, N.T.C. and M.D.; project administration, N.T.C. and M.D.; funding acquisition, M.D., I.M.F., N.T.C. and F.A. All authors have read and agreed to the published version of the manuscript.

Funding: This research was funded by the Associate Laboratory for Green Chemistry LAQV, which is financed by national funds from FCT/MEC (UID/QUI/50006/2019) and co-financed by the ERDF under the PT2020 Partnership Agreement (POCI-01-0145-FEDER—007265). This research was funded by the Interreg 2 Seas program 2014–2020, and co-funded by the European Regional Development Fund (FEDER) under subsidy contract 2S01-059_IMODE and 2S07-033_ Site Drug. This research was funded by the Program PHC PESSOA 2018 project nbr 4340/40868R. This research was funded by National Funds through FCT—Portuguese Foundation for Science and Technology, reference UIDB/00100/2020, UIDP/00100/2020, LA/P/0056/2020, UIDB/50025/2020-2023, and PTNMR (ROTEIRO/0031/2013; PINFRA/22161/2016), co-financed by ERDF through COMPETE 2020, Portugal, POCI and PORL and FCT through PIDDAC (POCI-01-0145-FEDER-007688). M.C.C. acknowledges PTNMR&i3N for the researcher contract. T. Cordeiro acknowledges Fundação para a Ciência e a Tecnologia (FCT) for the scholarship SFRH/BD/114653/2016. I. Matos acknowledges FCT for the Investigator FCT contract IF/01242/2014/CP1224/CT0008.

Institutional Review Board Statement: Not applicable.

Informed Consent Statement: Not applicable.

Data Availability Statement: Not applicable.

Acknowledgments: Simvastatin was a kind gift from Mepha Lda. "Investigação, Desenvolvimento e Fabricação Farmacêutica" (Porto Salvo, Portugal).

Conflicts of Interest: The authors declare no conflict of interest.

Appendix A

- FTIR results

The infrared spectrum collected for neat crystalline simvastatin in the carbonyl stretching region can be deconvoluted in three contributions, as shown in Figure A1: 1695.4, 1710 and 1725 cm^{-1} The first band is assigned to the stretching of hydrogen bonded (HB) carbonyl in the butyl ester tail, $C{=}O_{ester,HB}$ (1695 cm^{-1} [29]/1693.5 cm^{-1} [30]) that assures the infinite one dimensional chain along the crystallographic $\vec{b}$ axis: O3-H···O5 [44,58] (see SIM chemical structure and atoms numbering in Scheme 1). The area under the individual band is about one half of the total area (see Table A1), and so, the remaining two bands should be originated by stretching modes of the lactone carbonyl group, $C{=}O_{lact}$; these were also identified in the literature (1708 cm^{-1} and 1720 cm^{-1}) [29]. Two types of much weaker HB interactions involving lactone O2 assure the 2D and 3D molecular packing in crystalline SIM [44]: the C2−H···O2 interaction, having a 2.49 Å hydrogen bond distance, building a two dimensional sheet along the $\vec{c}$ axis, and the C9−H···O2 interaction, with 2.51 Å hydrogen bond distance, where chains arrange parallel with each other along the $\vec{a}$ axis. Having in mind the reported intermolecular hydrogen bond distances, it seems reasonable to assign the 1724.8 cm^{-1} and 1709.9 cm^{-1} bands, to vibrational modes associated with the lactone ring oxygen (O2) involved in, respectively, C9−H···O2 and C2−H···O2 interactions. The additive contribution of these two $C{=}O_{lact}$ bands is close to 50%, nevertheless, for a complete simulation of the overall band, two small contributions located at 1651 and

1618 cm^{-1} are necessary due to vibrations in the olefinic groups (C10=C11 and C12=C17), usually located in the range 1680–1620 cm^{-1} (asterisks in Figure A1).

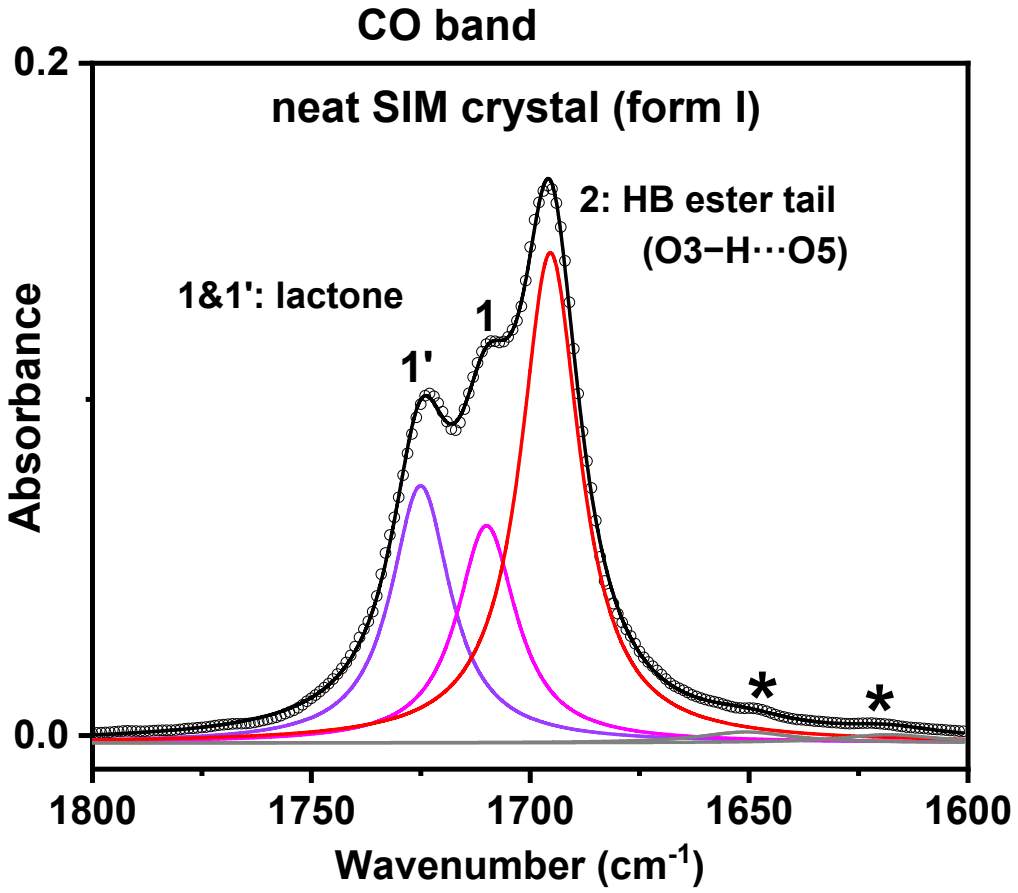

Figure A1. ATR-FTIR spectrum of neat SIM crystal polymorph I (room temperature), in the carbonyl stretching region.

Table A1. Summary of peak deconvolution of ATR-FTIR spectra in the 1800–1600 cm^{-1} wavenumber region, using a sum of Lorentz functions: position of the peak's maximum (max), width of the peak and relative area, A/A_{total}. * The peaks are identified in conformity with Figure A1.

Peak	Neat SIM Crystal	
	Max (Width) (cm^{-1})	**A/A_{total} (%)**
1′ ($C{=}O_{lact}$)	1725 (16.5)	47.7
1 ($C{=}O_{lact}$)	1710 (16.5)	
2 ($C{=}O_{ester}$)	1695 (16.5)	49.3
* (C=C)	1651 (26)	3
* (C=C)	1618 (27)	

- DSC results

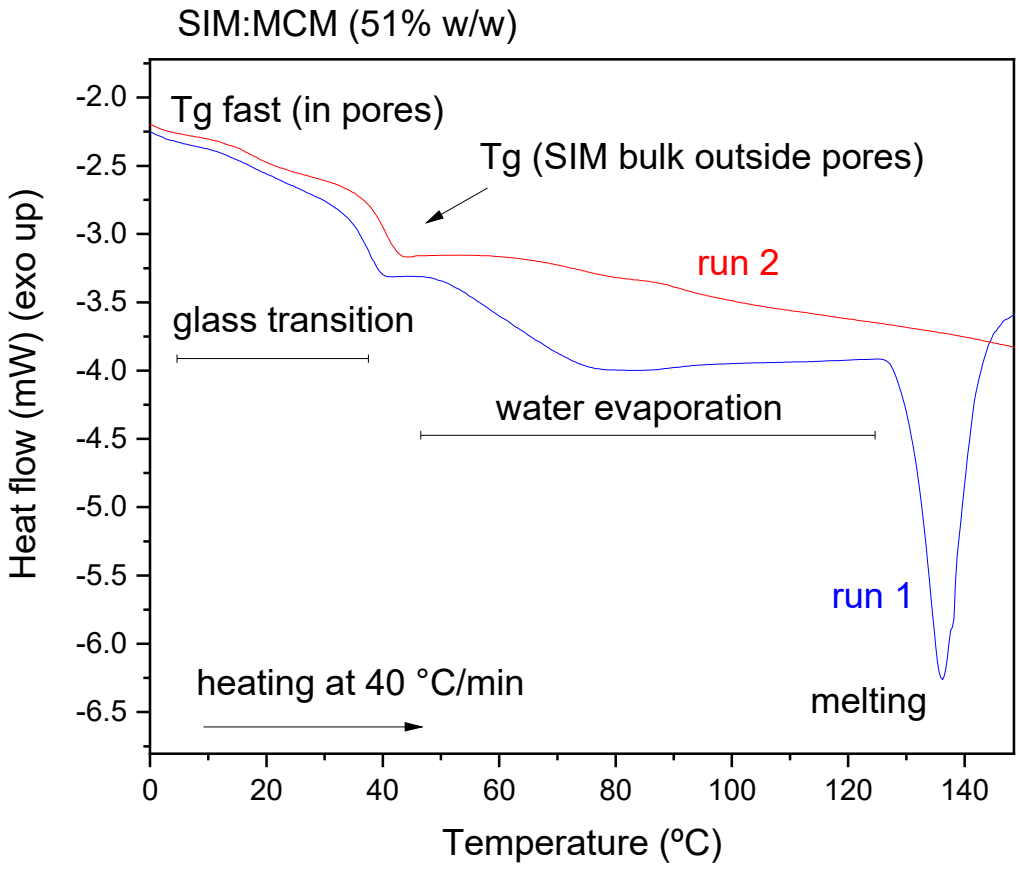

Figure A2. DSC curves obtained during heating of a SIM:MCM-41 composite with loading 51% (*w*/*w*).

- Dielectric results

Dielectric relaxation spectra of SIM:MCM, were collected isothermally in the temperature range from −95 °C to 165 °C, after a prior run carried out up to 100 °C to assure water release. The dielectric response expressed in terms of the real part of complex permittivity (ε') at 10^3 Hz, is represented in function of temperature (isochronal plot), respectively, by red open circles (first run) and filled blue circles (second run) in Figure A3. The final temperature of the first run was chosen also to avoid SIM evaporation, which starts immediately above 100 °C according to the thermogravimetric analysis of the composite (remember low-T vertical dashed line in Figure 3b). Concerning the two sets of SIM:MCM spectra, only a small difference is found between the corresponding traces in the temperature range where water evaporation occurs. If water would adsorb inside pores, it will gives rise to relaxational processes at lower temperatures (confined water), and it will greatly influence all dielectric spectrum due to the high dipole moment of water molecules, as shown for ibuprofen (hydrated vs. dehydrated composite [35]) incorporated in the same matrix. The absence of both effects in the SIM:MCM dielectric response means, on one side, that water in a small amount is present, as the FTIR analysis denotes, and as quantified by TGA; and, by other side, water is not relaxing in-pores, instead it is adsorbed in the outer surface. Therefore, dielectric spectroscopy provides evidence that pores are not accessible for water uptake, which is in agreement with the BET analysis that showed no N_2 adsorption in the composite.

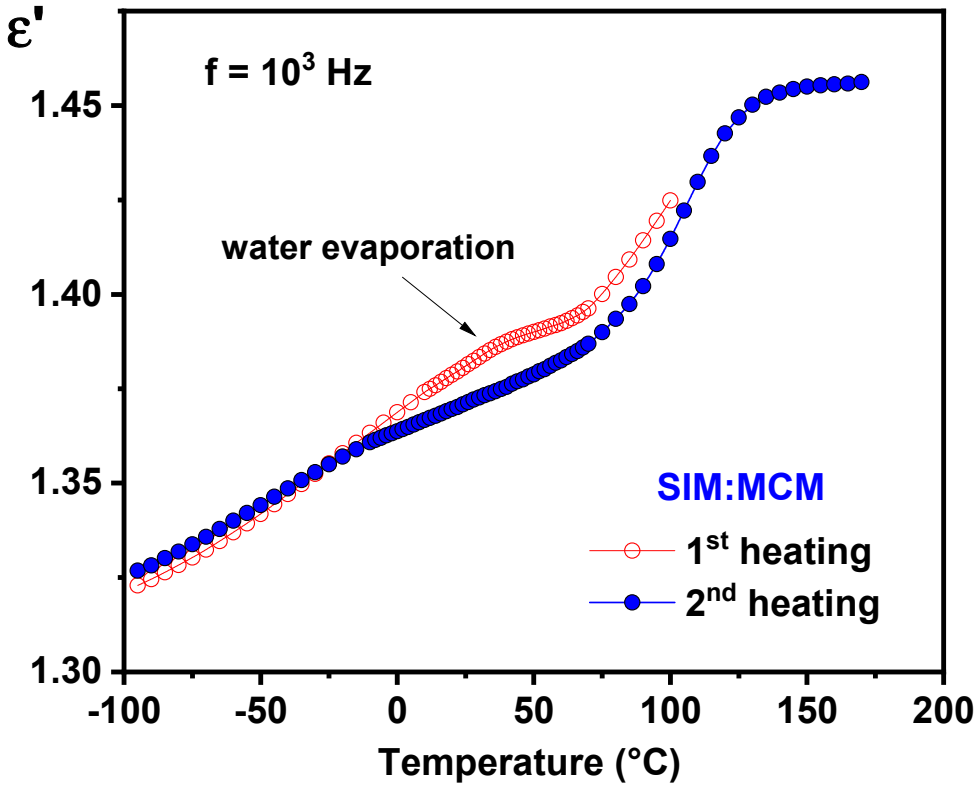

Figure A3. Isochronal plots of the real part of complex permittivity, $\varepsilon'(T)$, at 10^3 Hz, comparing 1st (hydrated) with 2nd (dehydrated) runs of SIM:MCM composite.

References

1. Kasim, N.A.; Whitehouse, M.; Ramachandran, C.; Bermejo, M.; Lennernäs, H.; Hussain, A.S.; Junginger, H.E.; Stavchansky, S.A.; Midha, K.K.; Shah, V.P.; et al. Molecular Properties of WHO Essential Drugs and Provisional Biopharmaceutical Classification. *Mol. Pharm.* **2004**, *1*, 85–96. [CrossRef]
2. DrugStats Database ClinCalc DrugStats Database. Available online: https://clincalc.com/DrugStats/ (accessed on 26 March 2023).
3. Ellison, D.K.; Moore, W.D.; Petts, C.R. Simvastatin. In *Analytical Profiles of Drug Substances and Excipients*; Brittain, H.G., Ed.; Elsevier: Amsterdam, The Netherlands, 1993; pp. 359–388.
4. Shitara, Y.; Sugiyama, Y. Pharmacokinetic and Pharmacodynamic Alterations of 3-Hydroxy-3-Methylglutaryl Coenzyme A (HMG-CoA) Reductase Inhibitors: Drug–Drug Interactions and Interindividual Differences in Transporter and Metabolic Enzyme Functions. *Pharmacol. Ther.* **2006**, *112*, 71–105. [CrossRef] [PubMed]
5. Jiang, T.; Han, N.; Zhao, B.; Xie, Y.; Wang, S. Enhanced Dissolution Rate and Oral Bioavailability of Simvastatin Nanocrystal Prepared by Sonoprecipitation. *Drug Dev. Ind. Pharm.* **2012**, *38*, 1230–1239. [CrossRef]
6. Serajuddin, A.T.M.; Ranadive, S.A.; Mahoney, E.M. Relative Lipophilicities, Solubilities, and Structure–Pharmacological Considerations of 3-Hydroxy-3-Methylglutaryl-Coenzyme A (HMG-CoA) Reductase Inhibitors Pravastatin, Lovastatin, Mevastatin, and Simvastatin. *J. Pharm. Sci.* **1991**, *80*, 830–834. [CrossRef] [PubMed]
7. Matsuyama, K.; Nakagawa, K.; Nakai, A.; Konishi, Y.; Nishikata, M.; Tanaka, H.; Uchida, T. Evaluation of Myopathy Risk for HMG-CoA Reductase Inhibitors by Urethane Infusion Method. *Biol. Pharm. Bull.* **2002**, *25*, 346–350. [CrossRef] [PubMed]
8. Jun, S.W.; Kim, M.-S.; Kim, J.-S.; Park, H.J.; Lee, S.; Woo, J.-S.; Hwang, S.-J. Preparation and Characterization of Simvastatin/Hydroxypropyl-β-Cyclodextrin Inclusion Complex Using Supercritical Antisolvent (SAS) Process. *Eur. J. Pharm. Biopharm.* **2007**, *66*, 413–421. [CrossRef] [PubMed]
9. Amidon, G.L.; Lennernäs, H.; Shah, V.P.; Crison, J.R. A Theoretical Basis for a Biopharmaceutic Drug Classification: The Correlation of in Vitro Drug Product Dissolution and in Vivo Bioavailability. *Pharm. Res.* **1995**, *12*, 413–420. [CrossRef]
10. Khadka, P.; Ro, J.; Kim, H.; Kim, I.; Kim, J.T.; Kim, H.; Cho, J.M.; Yun, G.; Lee, J. Pharmaceutical Particle Technologies: An Approach to Improve Drug Solubility, Dissolution and Bioavailability. *Asian J. Pharm. Sci.* **2014**, *9*, 304–316. [CrossRef]
11. Crowley, P.J.; Martini, L.G. Formulation Design: New Drugs from Old. *Drug Discov. Today Ther. Strateg.* **2004**, *1*, 537–542. [CrossRef]
12. Korani, S.; Bahrami, S.; Korani, M.; Banach, M.; Johnston, T.P.; Sahebkar, A. Parenteral Systems for Statin Delivery: A Review. *Lipids Health Dis.* **2019**, *18*, 193. [CrossRef]

13. Zidan, A.S.; Hosny, K.M.; Ahmed, O.A.A.; Fahmy, U.A. Assessment of Simvastatin Niosomes for Pediatric Transdermal Drug Delivery. *Drug Deliv.* **2016**, *23*, 1536–1549. [CrossRef]
14. Salem, H.F.; Kharshoum, R.M.; Abou-Taleb, H.A.; Farouk, H.O.; Zaki, R.M. Fabrication and Appraisal of Simvastatin via Tailored Niosomal Nanovesicles for Transdermal Delivery Enhancement: In Vitro and In Vivo Assessment. *Pharmaceutics* **2021**, *13*, 138. [CrossRef] [PubMed]
15. Chavhan, S.; Joshi, G.; Petkar, K.; Sawant, K. Enhanced Bioavailability and Hypolipidemic Activity of Simvastatin Formulations by Particle Size Engineering: Physicochemical Aspects and in Vivo Investigations. *Biochem. Eng. J.* **2013**, *79*, 221–229. [CrossRef]
16. Patel, J.K.; Sutariya, V.B. Micronisation of Simvastatin by the Supercritical Antisolvent Technique: In Vitro–in Vivo Evaluation. *J. Microencapsul.* **2015**, *32*, 193–200. [CrossRef] [PubMed]
17. Padhye, S.G.; Nagarsenker, M.S. Simvastatin Solid Lipid Nanoparticles for Oral Delivery: Formulation Development and In Vivo Evaluation. *Indian J. Pharm. Sci.* **2013**, *75*, 591–598. [PubMed]
18. Rao, M.; Mandage, Y.; Thanki, K.; Bhise, S. Dissolution Improvement of Simvastatin by Surface Solid Dispersion Technology. *Dissolution Technol.* **2010**, *17*, 27–34. [CrossRef]
19. Pandya, P.; Gattani, S.; Jain, P.; Khirwal, L.; Surana, S. Co-Solvent Evaporation Method for Enhancement of Solubility and Dissolution Rate of Poorly Aqueous Soluble Drug Simvastatin: In Vitro–In Vivo Evaluation. *AAPS PharmSciTech* **2008**, *9*, 1247–1252. [CrossRef]
20. Kang, B.K.; Lee, J.S.; Chon, S.K.; Jeong, S.Y.; Yuk, S.H.; Khang, G.; Lee, H.B.; Cho, S.H. Development of Self-Microemulsifying Drug Delivery Systems (SMEDDS) for Oral Bioavailability Enhancement of Simvastatin in Beagle Dogs. *Int. J. Pharm.* **2004**, *274*, 65–73. [CrossRef]
21. Bannow, J.; Yorulmaz, Y.; Löbmann, K.; Müllertz, A.; Rades, T. Improving the Drug Load and in Vitro Performance of Supersaturated Self-Nanoemulsifying Drug Delivery Systems (Super-SNEDDS) Using Polymeric Precipitation Inhibitors. *Int. J. Pharm.* **2020**, *575*, 118960. [CrossRef]
22. Craye, G.; Löbmann, K.; Grohganz, H.; Rades, T.; Laitinen, R. Characterization of Amorphous and Co-Amorphous Simvastatin Formulations Prepared by Spray Drying. *Molecules* **2015**, *20*, 21532–21548. [CrossRef]
23. Redzuan Meor Mohd Affandi, M.M.; Tripathy, M.; Majeed, A.B.A. Arginine Complexes with Simvastatin: Apparent Solubility, In Vitro Dissolution and Solid State Characterization. *Curr. Drug Deliv.* **2018**, *15*, 77–86. [CrossRef]
24. Ambike, A.A.; Mahadik, K.R.; Paradkar, A. Spray-Dried Amorphous Solid Dispersions of Simvastatin, a Low Tg Drug: In Vitro and in Vivo Evaluations. *Pharm. Res.* **2005**, *22*, 990–998. [CrossRef]
25. Ambike, A.A.; Mahadik, K.R.; Paradkar, A. Physico-Chemical Characterization and Stability Study of Glassy Simvastatin. *Drug Dev. Ind. Pharm.* **2005**, *31*, 895–899. [CrossRef] [PubMed]
26. Nunes, T.G.; Viciosa, M.T.; Correia, N.T.; Danède, F.; Nunes, R.G.; Diogo, H.P. A Stable Amorphous Statin: Solid-State NMR and Dielectric Studies on Dynamic Heterogeneity of Simvastatin. *Mol. Pharm.* **2014**, *11*, 727–737. [CrossRef]
27. Graeser, K.A.; Strachan, C.J.; Patterson, J.E.; Gordon, K.C.; Rades, T. Physicochemical Properties and Stability of Two Differently Prepared Amorphous Forms of Simvastatin. *Cryst. Growth Des.* **2008**, *8*, 128–135. [CrossRef]
28. Zhang, F.; Aaltonen, J.; Tian, F.; Saville, D.; Rades, T. Influence of Particle Size and Preparation Methods on the Physical and Chemical Stability of Amorphous Simvastatin. *Eur. J. Pharm. Biopharm.* **2009**, *71*, 64–70. [CrossRef] [PubMed]
29. Modhave, D.; Saraf, I.; Karn, A.; Paudel, A. Understanding Concomitant Physical and Chemical Transformations of Simvastatin During Dry Ball Milling. *AAPS PharmSciTech* **2020**, *21*, 152. [CrossRef] [PubMed]
30. Löbmann, K.; Strachan, C.; Grohganz, H.; Rades, T.; Korhonen, O.; Laitinen, R. Co-Amorphous Simvastatin and Glipizide Combinations Show Improved Physical Stability without Evidence of Intermolecular Interactions. *Eur. J. Pharm. Biopharm.* **2012**, *81*, 159–169. [CrossRef] [PubMed]
31. Nandi, U.; Ajiboye, A.L.; Patel, P.; Douroumis, D.; Trivedi, V. Preparation of Solid Dispersions of Simvastatin and Soluplus Using a Single-Step Organic Solvent-Free Supercritical Fluid Process for the Drug Solubility and Dissolution Rate Enhancement. *Pharmaceuticals* **2021**, *14*, 846. [CrossRef] [PubMed]
32. Xiao, J.; Wan, Y.; Yang, Z.; Huang, Y.; Yao, F.; Luo, H. Bioactive Glass Nanotube Scaffold with Well-Ordered Mesoporous Structure for Improved Bioactivity and Controlled Drug Delivery. *J. Mater. Sci. Technol.* **2019**, *35*, 1959–1965. [CrossRef]
33. Song, K.; Tang, Z.; Song, Z.; Meng, S.; Yang, X.; Guo, H.; Zhu, Y.; Wang, X. Hyaluronic Acid-Functionalized Mesoporous Silica Nanoparticles Loading Simvastatin for Targeted Therapy of Atherosclerosis. *Pharmaceutics* **2022**, *14*, 1265. [CrossRef]
34. Knapik-Kowalczuk, J.; Kramarczyk, D.; Chmiel, K.; Romanova, J.; Kawakami, K.; Paluch, M. Importance of Mesoporous Silica Particle Size in the Stabilization of Amorphous Pharmaceuticals—The Case of Simvastatin. *Pharmaceutics* **2020**, *12*, 384. [CrossRef]
35. Inocêncio, S.; Cordeiro, T.; Matos, I.; Danède, F.; Sotomayor, J.C.; Fonseca, I.M.; Correia, N.T.; Corvo, M.C.; Dionísio, M. Ibuprofen Incorporated into Unmodified and Modified Mesoporous Silica: From Matrix Synthesis to Drug Release. *Microporous Mesoporous Mater.* **2021**, *310*, 110541. [CrossRef]
36. Varache, M.; Bezverkhyy, I.; Saviot, L.; Bouyer, F.; Baras, F.; Bouyer, F. Optimization of MCM-41 Type Silica Nanoparticles for Biological Applications: Control of Size and Absence of Aggregation and Cell Cytotoxicity. *J. Non. Cryst. Solids* **2015**, *408*, 87–97. [CrossRef]
37. Shevtsov, M.A.; Parr, M.A.; Ryzhov, V.A.; Zemtsova, E.G.; Arbenin, A.Y.; Ponomareva, A.N.; Smirnov, V.M.; Multhoff, G. Zero-Valent Fe Confined Mesoporous Silica Nanocarriers (Fe(0) @ MCM-41) for Targeting Experimental Orthotopic Glioma in Rats. *Sci. Rep.* **2016**, *6*, 29247. [CrossRef] [PubMed]

38. Skwira, A.; Szewczyk, A.; Konopacka, A.; Górska, M.; Majda, D.; Sądej, R.; Prokopowicz, M. Silica-Polymer Composites as the Novel Antibiotic Delivery Systems for Bone Tissue Infection. *Pharmaceutics* **2019**, *12*, 28. [CrossRef]
39. Alharthi, S.; Ziora, Z.M.; Janjua, T.; Popat, A.; Moyle, P.M. Formulation and Biological Evaluation of Mesoporous Silica Nanoparticles Loaded with Combinations of Sortase A Inhibitors and Antimicrobial Peptides. *Pharmaceutics* **2022**, *14*, 986. [CrossRef]
40. D'Orey, P.; Cordeiro, T.; Lourenço, M.A.O.; Matos, I.; Danède, F.; Sotomayor, J.C.; Fonseca, I.M.; Ferreira, P.; Correia, N.T.; Dionísio, M. How Molecular Mobility, Physical State, and Drug Distribution Influence the Naproxen Release Profile from Different Mesoporous Silica Matrices. *Mol. Pharm.* **2021**, *18*, 898–914. [CrossRef]
41. Schönhals, A.; Kremer, F. Theory of Dielectric Relaxation. In *Broadband Dielectric Spectroscopy*; Kremer, F., Schönhals, A., Eds.; Springer Berlin Heidelberg: Berlin/Heidelberg, Germany, 2003; pp. 1–33.
42. Villarroel Rocha, J.; Barrera, D.; Sapag, K. Improvement in the Pore Size Distribution for Ordered Mesoporous Materials with Cylindrical and Spherical Pores Using the Kelvin Equation. *Top. Catal.* **2011**, *54*, 121–134. [CrossRef]
43. Barrett, E.P.; Joyner, L.G.; Halenda, P.P. The Determination of Pore Volume and Area Distributions in Porous Substances. I. Computations from Nitrogen Isotherms. *J. Am. Chem. Soc.* **1951**, *73*, 373–380. [CrossRef]
44. Simões, R.G.; Bernardes, C.E.S.; Joseph, A.; Piedade, M.F.M.; Kraus, W.; Emmerling, F.; Diogo, H.P.; Minas da Piedade, M.E. Polymorphism in Simvastatin: Twinning, Disorder, and Enantiotropic Phase Transitions. *Mol. Pharm.* **2018**, *15*, 5349–5360. [CrossRef] [PubMed]
45. McCrum, N.; Williams, B.; Read, G. *Anelastic and Dielectric Effects in Polymeric Solids*; Wiley: New York, NY, USA, 1967; ISBN 978-0486667522.
46. Smith, W.; Forester, T.R.; Todorov, I.T. *The DL POLY Classic User Manual*; 1.9; Daresbury Laboratory: Warrington, UK, 2012.
47. Vink, R.L.C.; Barkema, G.T. Large Well-Relaxed Models of Vitreous Silica, Coordination Numbers, and Entropy. *Phys. Rev. B* **2003**, *67*, 245201. [CrossRef]
48. Bródka, A.; Zerda, T.W. Properties of Liquid Acetone in Silica Pores: Molecular Dynamics Simulation. *J. Chem. Phys.* **1996**, *104*, 6319–6326. [CrossRef]
49. Puibasset, J.; Pellenq, R.J.-M. Grand Canonical Monte Carlo Simulation Study of Water Structure on Hydrophilic Mesoporous and Plane Silica Substrates. *J. Chem. Phys.* **2003**, *119*, 9226–9232. [CrossRef]
50. Busselez, R.; Lefort, R.; Ji, Q.; Affouard, F.; Morineau, D. Molecular Dynamics Simulation of Nanoconfined Glycerol. *Phys. Chem. Chem. Phys.* **2009**, *11*, 11127–11133. [CrossRef]
51. Jorgensen, W.L.; Maxwell, D.S.; Tirado-Rives, J. Development and Testing of the OPLS All-Atom Force Field on Conformational Energetics and Properties of Organic Liquids. *J. Am. Chem. Soc.* **1996**, *118*, 11225–11236. [CrossRef]
52. Costa, J.A.S.; de Jesus, R.A.; da Silva, C.M.P.; Romão, L.P.C. Efficient Adsorption of a Mixture of Polycyclic Aromatic Hydrocarbons (PAHs) by Si–MCM–41 Mesoporous Molecular Sieve. *Powder Technol.* **2017**, *308*, 434–441. [CrossRef]
53. Azaïs, T.; Tourné-Péteilh, C.; Aussenac, F.; Baccile, N.; Coelho, C.; Devoisselle, J.-M.; Babonneau, F. Solid-State NMR Study of Ibuprofen Confined in MCM-41 Material. *Chem. Mater.* **2006**, *18*, 6382–6390. [CrossRef]
54. Cheng, Y.-J.; Zhang, A.-Q.; Hu, J.-J.; He, F.; Zeng, X.; Zhang, X.-Z. Multifunctional Peptide-Amphiphile End-Capped Mesoporous Silica Nanoparticles for Tumor Targeting Drug Delivery. *ACS Appl. Mater. Interfaces* **2017**, *9*, 2093–2103. [CrossRef]
55. Rahoui, N.; Jiang, B.; Hegazy, M.; Taloub, N.; Wang, Y.; Yu, M.; Huang, Y.D. Gold Modified Polydopamine Coated Mesoporous Silica Nano-Structures for Synergetic Chemo-Photothermal Effect. *Colloids Surf. B Biointerfaces* **2018**, *171*, 176–185. [CrossRef]
56. Dressaire, E.; Sauret, A. Clogging of Microfluidic Systems. *Soft Matter* **2017**, *13*, 37–48. [CrossRef] [PubMed]
57. Bouhid de Aguiar, I.; Schroën, K. Microfluidics Used as a Tool to Understand and Optimize Membrane Filtration Processes. *Membranes* **2020**, *10*, 316. [CrossRef] [PubMed]
58. Čejka, J.; Kratochvíl, B.; Císařová, I.; Jegorov, A. Simvastatin. *Acta Crystallogr. Sect. C Cryst. Struct. Commun.* **2003**, *C59*, o428–o430. [CrossRef]
59. Hušák, M.; Kratochvíl, B.; Jegorov, A.; Brus, J.; Maixner, J.; Rohlíček, J. Simvastatin: Structure Solution of Two New Low-Temperature Phases from Synchrotron Powder Diffraction and ss-NMR. *Struct. Chem.* **2010**, *21*, 511–518. [CrossRef]
60. Brus, J.; Jegorov, A. Through-Bonds and Through-Space Solid-State NMR Correlations at Natural Isotopic Abundance: Signal Assignment and Structural Study of Simvastatin. *J. Phys. Chem. A* **2004**, *108*, 3955–3964. [CrossRef]
61. Silverstein, R.M.; Bassler, G.C.; Morril, T.C. *Spectrometric Identification of Organic Compounds*; John Wiley & Sons: New York, NY, USA, 1991; ISBN 0471 63404 2.
62. Simões, R.G.; Bernardes, C.E.S.; Diogo, H.P.; Agapito, F.; Minas da Piedade, M.E. Energetics and Structure of Simvastatin. *Mol. Pharm.* **2013**, *10*, 2713–2722. [CrossRef]
63. Kremer, F.; Huwe, A.; Schönhals, A.; Różański, S.A. Molecular Dynamics in Confining Space. In *Broadband Dielectric Spectroscopy*; Kremer, F., Schönhals, A., Eds.; Springer Berlin Heidelberg: Berlin/Heidelberg, Germany, 2003; pp. 171–224.
64. Wübbenhorst, M.; Napolitano, S. Deviations from Bulk Glass Transition Dynamics of Small Molecule Glass Formers: Some Scenarios in Relation to the Dimensionality of the Confining Geometry. In *Dynamics in geometrical confinement*; Kremer, F., Ed.; Springer: Berlin/Heidelberg, Germany, 2014; pp. 247–277.
65. Richert, R. Dynamics of Nanoconfined Supercooled Liquids. *Annu. Rev. Phys. Chem.* **2011**, *62*, 65–84. [CrossRef] [PubMed]

66. Dionísio, M.; Correia, N.T.; Brás, A.R. Molecular Mobility and Phase Transformations of Several Low Molecular Weight Glass Formers Confined to Nanoporous Silica Matrices. In *Dynamics in Geometrical Confinement*; Kremer, F., Ed.; Springer: Berlin/Heidelberg, Germany, 2014; pp. 213–245.
67. Steeman, P.A.M.; van Turnhout, J. Dielectric Properties of Inhomogeneous Media. In *Broadband Dielectric Spectroscopy*; Kremer, F., Schönhals, A., Eds.; Springer Berlin Heidelberg: Berlin/Heidelberg, Germany, 2003; pp. 495–522.
68. Horstmann, R.; Hecht, L.; Kloth, S.; Vogel, M. Structural and Dynamical Properties of Liquids in Confinements: A Review of Molecular Dynamics Simulation Studies. *Langmuir* **2022**, *38*, 6506–6522. [CrossRef]
69. Renou, R.; Szymczyk, A.; Ghoufi, A. Water Confinement in Nanoporous Silica Materials. *J. Chem. Phys.* **2014**, *140*, 044704. [CrossRef]